

# Quantifying urban, industrial, and background changes in NO<sub>2</sub> during the COVID-19 lockdown period based on TROPOMI satellite observations

5 Vitali Fioletov<sup>1</sup>, Chris A. McLinden<sup>1</sup>, Debora Griffin<sup>1</sup>, Nickolay Krotkov<sup>2</sup>, Fei Liu<sup>2</sup>, Henk Eskes<sup>3</sup>

<sup>1</sup>Air Quality Research Division, Environment and Climate Change Canada, Toronto, Canada

<sup>2</sup>Atmospheric Chemistry and Dynamics Laboratory, NASA Goddard Space Flight Center, Greenbelt, Maryland, USA

<sup>3</sup>Royal Netherlands Meteorological Institute, De Bilt, the Netherlands

10

*Correspondence to:* Vitali Fioletov (Vitali.Fioletov@outlook.com or [Vitali.Fioletov@ec.gc.ca](mailto:Vitali.Fioletov@ec.gc.ca))

**Abstract.** The COVID-19 lockdown had a large impact on anthropogenic emissions of air pollutants and particularly on nitrogen dioxide (NO<sub>2</sub>). While the overall NO<sub>2</sub> decline over some large cities is well-established, understanding the details remains a challenge since multiple source categories contribute. In this study, a new method of isolation of three components: background NO<sub>2</sub>, NO<sub>2</sub> from urban sources, and from industrial point sources is applied to estimate the impact of the COVID-19 lockdown on each of them. The approach is based on fitting satellite data by a statistical model with empirical plume dispersion functions driven by a meteorological reanalysis. Population density and surface elevation data as well as coordinates of industrial sources were used in the analysis. The tropospheric NO<sub>2</sub> vertical column density (VCD) values measured by the Tropospheric Monitoring Instrument (TROPOMI) on board Sentinel-5 Precursor over 261 (3° by 4°) urban areas for the period from March 16 to June 15, 2020, were compared with the average VCD values for the same period in 2018 and 2019. While background NO<sub>2</sub> component remained almost unchanged, the urban NO<sub>2</sub> component declined by -18% to -28% over most regions. India, South America, and a part of Europe (particularly, Italy, France, and Spain) demonstrated a -40% to -50% urban emissions decline. In contrast, the decline over urban areas in China, where the lockdown was over during the analyzed period, was, on average, only -4.4%±8%. Emissions from large industrial sources in the analyzed urban areas varied largely from region to region from -4.8%±6% for China to -40%±10% for India. Estimated changes in urban emissions are correlated with changes in Google mobility data (the correlation coefficient is 0.62) confirming that changes in traffic was one of the key elements in decline of urban NO<sub>2</sub> emissions. No correlation was found between changes in background NO<sub>2</sub> and Google mobility data. On the global scale, the background and urban component were remarkably stable in 2018, 2019, and 2021, with averages of all analysed areas being all within ±2.5% and suggesting that there were no substantial drifts or shifts in TROPOMI data. The 2020 data are clearly an outlier: in 2020, the mean background component for all analysed areas (without China) was -6.0%±1.2% and the mean urban component was -26.7%±2.6% or 20-σ below the baseline level from the other years.

## 1 Introduction

Nitrogen oxides ( $\text{NO}_x = \text{NO}_2 + \text{NO}$ ) are air pollutants that originate from various anthropogenic (fuel combustion) and natural (e.g., biomass burning, lightning) sources and whose emissions are regulated in many countries. Satellite measurements of one component of  $\text{NO}_x$ ,  $\text{NO}_2$  have a long history. In the stratosphere, the SAGE (Stratospheric Aerosol and Gas Experiment) instrument provided  $\text{NO}_2$  profile information through the stratosphere beginning in the mid-1980s (Cunnold et al., 1991). Satellite observations of tropospheric  $\text{NO}_2$  columns are more recent and began with the nadir-viewing GOME (Global Ozone Monitoring Experiment) in 1996 (Martin et al., 2002) with several successors, chief among these OMI (Ozone Monitoring Instrument) (Duncan et al., 2015; Krotkov et al., 2016; Lamsal et al., 2015, 2021; Levelt et al., 2018) and, most recently, TROPOMI (Tropospheric Monitoring Instrument) (van Geffen et al., 2020; Veefkind et al., 2012). Collectively these instruments have been used to better understand  $\text{NO}_2$  sources, sinks, distributions, and trends (Beirle et al., 2011, 2019; Liu et al., 2016; Lorente et al., 2019; Lu et al., 2015; Martin et al., 2002; McLinden et al., 2012; Stavrakou et al., 2020; Vîrghileanu et al., 2020) .

One primary  $\text{NO}_2$  characteristic provided by satellites is tropospheric vertical column density (VCD), a geophysical quantity representing the total number of molecules or total mass per unit of area in the troposphere. The main features of the tropospheric  $\text{NO}_2$  VCD distribution are well established. Due to its relatively short lifetime, a few hours within a plume during the day,  $\text{NO}_2$  is elevated near sources such as urban areas (Beirle et al., 2019; Lorente et al., 2019; Lu et al., 2015) and industrial locations such as power plants and oil refineries (Liu et al., 2016; McLinden et al., 2012). Over high mountains,  $\text{NO}_2$  VCDs are relatively small as the troposphere there is “thinner” with fewer emissions sources. Ship tracks and major highways also create elevated  $\text{NO}_2$  values on satellite maps (Beirle et al., 2004; Georgoulas et al., 2020; Liu et al., 2020a; Richter et al., 2004).

The COVID-19 lockdown had an impact on tropospheric  $\text{NO}_2$  levels, first in China and then worldwide (Bao and Zhang, 2020; Bauwens et al., 2020; Ding et al., 2020; Gkatzelis et al., 2021; Kanniah et al., 2020; Keller et al., 2021; Koukouli et al., 2021; Liu et al., 2020a; Vadrevu et al., 2020; Vîrghileanu et al., 2020; Zhang et al., 2021). It was demonstrated that  $\text{NO}_2$  surface concentrations and VCDs have significantly declined in the U.S. and Canada after mid-March 2020 (Bauwens et al., 2020; Goldberg et al., 2020; Griffin et al., 2020). A decline of about -20% to -25% was observed in the U.S. megacities, as well as over some rural areas. A decline was also reported over Europe (e.g., Bar et al., 2021; Barré et al., 2021), India (Mirsa et al., 2021; Hassan et al., 2021), Pakistan (Ghaffar et al., 2021; Mehmood et al., 2021), Brazil (Dantas et al., 2020; Siciliano et al., 2020), and other parts of the world (Ass et al., 2020; Aydin et al., 2020; Fu et al., 2020) as also discussed in overview papers (Gkatzelis et al., 2021; Levelt et al., 2021).

The impact of the lockdown on tropospheric  $\text{NO}_2$  VCD from satellite data was often estimated by comparing mean or median values over a certain area for the periods before and after the lockdown (e.g., Qu, et al., 2021; Barré et al., 2021; Mehmood et al., 2021; Hassan et al., 2021; see also online tool [https://so2.gsfc.nasa.gov/no2/no2\\_index.html](https://so2.gsfc.nasa.gov/no2/no2_index.html) accessed Dec. 18, 2021) or as the values weighted according to the population density (Sannigrahi et al., 2021). This makes the results

dependent on the area analyzed and sensitive to the wind speed (Goldberg et al., 2021). There is also free tropospheric NO<sub>2</sub> that could mask the lockdown-related changes in anthropogenic emissions (Silvern et al., 2019). Moreover, meteorological variability was also a contributing factor to the differences (e.g., Barré et al., 2021; Griffin et al., 2020) although some studies found that its impact may not be very large (Bar et al., 2021).

5 An alternative approach is based on estimation of NO<sub>2</sub> emissions using satellite data and then comparing the emissions estimates before and after the lockdown started (Lange et al., 2021). There are several methods to estimate the emissions (Streets et al., 2013). Methods such as inverse modelling (Konovalov et al., 2006; Mijling and van Der A, 2012) and, more recently, flux divergence (Beirle et al., 2019; 2021) are used for such purpose. One common technique is based on a rotation of satellite NO<sub>2</sub> pixels around the source so the NO<sub>2</sub> data would appear if the wind is from one common direction, allowing  
10 many overpasses to be combined. These rotated data are then integrated in the cross-wind direction and then fitting the results with an exponentially modified Gaussian (EMG) function (Lange et al., 2021; Pommier et al., 2013). The two unknown parameters, the emission strength and lifetime are estimated directly from the fit in one-dimensional space. The method works well for isolated stationary point sources and with steady winds (Beirle et al., 2021) but may not work in the areas where emissions from closely located multiple sources are mixed with urban emissions. Another approach employs a two-dimensional  
15 EMG plume function of the wind speed (Dammers et al., 2019; Fioletov et al., 2015, McLinden et al., 2020). The plume function depends on three parameters: the plume width, lifetime, and emission strengths. While all three parameters can be estimated from the fit, the algorithm works better if the plume width and lifetime are estimated in advance and then prescribed in the fit to estimate the emission strength. This algorithm was further improved to account for multiple sources or area (Fioletov et al., 2017).

20 A different approach was used in this study. A statistical model was used to describe the TROPOMI NO<sub>2</sub> data over 3° by 4° areas (roughly, 330 km by 330 km at 42°N) around major cities and isolate three components related to (1) plumes from urban sources, (2) plumes from industrial point sources, and (3) background NO<sub>2</sub>. The parameters of the statistical model link the satellite NO<sub>2</sub> values to proxies related to elevation and population density as well as to locations of large industrial point sources. Then the three components in 2020 were compared to their values in 2018-2019 to study the COVID-19  
25 lockdown impact. The parameters have simple physical interpretation such as point source or area emission rates and the background NO<sub>2</sub> distribution. As the model has only a few parameters and their estimates are based on several hundreds of TROPOMI pixels in each area, statistical uncertainties of the parameter estimates are very small. The variability of urban, industrial, and background NO<sub>2</sub> components due to meteorological or observational conditions was studied by comparing the estimates of the three components for 2018, 2019, and 2021 that were not affected by lockdowns.

30 This algorithm is based on a multisource plume dispersion function fitting approach developed for sulfur dioxide (SO<sub>2</sub>) point and area sources (Fioletov et al., 2017; McLinden et al., 2020). It assumes that each source produces a plume that depends on unknown emission strength and these emission strengths are derived from the best fit to the satellite data. The algorithm was adapted for NO<sub>2</sub> where emissions from urban areas, which tend to be dominated by residential and mobile emission sources, were often a major source sector. Since the approach is based on statistical methods it was necessary to

have a sufficiently long data set to reduce the impact of natural factors such as meteorology that can cause NO<sub>2</sub> VCD differences of ~15% over monthly timescales (Goldberg et al., 2020; Levelt et al., 2021). We use three-month periods, with the averages for the period from March 16 to June 15, 2020, are compared to those in 2018 and 2019 for the 3° by 4° areas around 261 major cities worldwide. As the study is focused on relative NO<sub>2</sub> changes due to the lockdown, possible systematic errors related to the TROPOMI retrievals (Verhoelst et al., 2021) and the algorithm fitting parameters (Fioletov et al., 2016) play a much smaller role than in the case of absolute emission estimates.

This paper is organized as follows: Section 2 describes various data sets used in the study; the analysis algorithm is discussed in Section 3. In Section 4, the COVID-19 lockdown impact is studied. USA and Canada are analyzed in detail to illustrate the method, then statistics for Europe are provided and finally results for the entire world are presented. Discussion and conclusions are given in Section 5. The algorithm is described in Appendix. Additional technical information and statistics are given in the Supplement.

## 2 Data Sets

### 2.1 TROPOMI NO<sub>2</sub> VCD data

TROPOMI, onboard of the European Space Agency (ESA) and EU Copernicus Sentinel 5 Precursor (S5p) satellite, was launched on 13 October 2017 (van Geffen et al., 2020; Veefkind et al., 2012). The satellite follows a Sun-synchronous, low-Earth (825 km) orbit with a daily equator crossing time of approximately 13:30 local solar time (van Geffen et al., 2019). At nadir, TROPOMI pixel sizes were  $3.5 \times 7 \text{ km}^2$  at the beginning of operation and were reduced to  $3.5 \times 5.6 \text{ km}^2$  on 6 August 2019 and the swath width is 2,600 km. TROPOMI NO<sub>2</sub> VCD values represent the total number of molecules or total mass per unit area below tropopause and are often given in molecules or moles (one mole is equal to  $6.022 \times 10^{23}$  molecules) per square metre or centimetre as well as in Dobson Units (DU,  $1 \text{ DU} = 2.69 \times 10^{16} \text{ molec cm}^{-2}$ ). In this study, level 2 TROPOMI data available from the Copernicus open data access hub (<https://s5phub.copernicus.eu>) were used. The reprocessed (RPRO) data version V1.2.2 was used for 2018 and offline mode (OFFL) data of version V1.2.2 to version V1.3.2 were used for 2019-2020. The difference between these two versions is relatively minor, and therefore the combination is suitable to analyse NO<sub>2</sub> changes during the period studied in this paper. The 2021 data (V1.4.0) were used only to estimate the interannual variability. The standard TROPOMI product, tropospheric vertical columns, based on air mass factors (AMFs) calculated using the vertical profile of NO<sub>2</sub> from the TM5-MP model at  $1^\circ \times 1^\circ$  resolution (Williams et al., 2017) was used. In the analysis, we use only data for which the quality assurance value is higher than 0.75 (van Geffen et al., 2018). Also, satellite pixels with snow on the ground, a solar zenith angle greater than 75 degrees and with cloud radiance fraction above 0.3 were excluded from the analysis.

The specified random uncertainty of a single TROPOMI tropospheric NO<sub>2</sub> VCD measurement is  $7 \times 10^{14} \text{ molec cm}^{-2}$  (or 0.026 DU) (ESA EOP-GMQ, 2017). Tack et al., (2021) estimated this uncertainty and found it to be  $5.6 \pm 0.4 \times 10^{14} \text{ molec cm}^{-2}$ . There is some evidence that TROPOMI NO<sub>2</sub> is biased low by 14%-40% over polluted areas due to a limited spatial resolution of the model used to calculate the AMFs (Judd et al., 2020; Verhoelst et al., 2021; Zhao et al.,

2020). This bias can be reduced by recalculation of AMFs with higher spatial resolution (Griffin et al., 2020; Ialongo et al., 2020; Zhao et al., 2020; Tack et al., 2021). In addition, the cloud pressures derived from the TROPOMI data have a positive bias in versions 1.2.x and 1.3.x which has an impact on the NO<sub>2</sub> tropospheric column retrieved (van Geffen et al., 2021). Both effects (biases) are expected to scale roughly linearly with the column amount (van Geffen et al., 2021), consistent with the validation results (Verhoelst et al., 2021). Therefore, the relative differences between 2018-2019 and 2020 data studied here, should not be affected by these effects.

The TROPOMI NO<sub>2</sub> distribution over the US and southern Canada is shown in Fig.1. The data are stratified by the wind speed to highlight some of the features of the NO<sub>2</sub> VCD distribution. NO<sub>2</sub> values are elevated over highly populated areas, as is particularly evident from the maps for low wind speed where the NO<sub>2</sub> remains close to the source before chemical or physical removal. Fig.1 also illustrates the fact that TROPOMI NO<sub>2</sub> values over megacities are higher under calm winds and lower under high winds (e.g., Goldberg et al., 2020). Elevated NO<sub>2</sub> values are also observed over power plants and mining operations (Goldberg et al., 2021). The NO<sub>2</sub> VCD distribution also depends on local topography (Kim et al., 2021). For example, smaller values over elevated areas such as the Rocky Mountains and Appalachians and higher values over valleys such the California Central Valley are evident from the map. There is also some background NO<sub>2</sub> that can be seen even over remote areas with no major anthropogenic sources: NO<sub>2</sub> VCDs are not negligible (about  $5 \cdot 10^{14} \text{ cm}^{-2}$ ) over vast remote areas such as National Forests in Montana or Algonquin Provincial Park in Ontario as well as over the oceans.

As TROPOMI has only one daily overpass at most locations, diurnal NO<sub>2</sub> variations may affect emissions estimates. Measurements from the ground demonstrate, that unlike surface concentrations, the diurnal variations of NO<sub>2</sub> VCDs are relatively small, particularly in spring (Herman et al., 2009; Chong et al., 2018). However, since night time NO<sub>2</sub> information is not available from satellite, we should say that all the results presented here are limited to daytime emissions only.

## 2.2 Wind data

As in several previous studies (Fioletov et al., 2015; McLinden et al., 2020; Zoogman et al., 2016) the plume dispersion function (discussed below in Sect. 3) is based on the wind speed and direction obtained from the meteorological reanalysis. For each satellite pixel, wind speed and direction were calculated based on European Centre for Medium-Range Weather Forecasts (ECMWF) ERA5 reanalysis data (C3S, 2017; Dee et al., 2011), which were merged with TROPOMI measurements. The wind profile data have one hour temporal resolution and are available on a 0.25° horizontal grid. U- and V- (west-east and south-north, respectively) wind-speed components were then linearly interpolated to the location of the centre of each TROPOMI pixel and to overpass time. The ERA5 wind components at 1000, 950, and 900 hPa were averaged to obtain the used wind value (that approximately corresponds to the mean winds between 0 and 1 km). This interval was comparable to the wind data used in other similar studies: Beirle et al. (2019) used data at 450 m, while Lange et al., (2021), used data from 100 m. The results are not very sensitive to the wind profile within this range as was previously investigated by Beirle et al., (2011) because the boundary layer wind is relatively constant, except close to the surface. Note that in ERA5 reanalysis in pressure

co-ordinates, when the surface pressure is smaller than that at a given level (e.g., 1000 hPa) the values will simply duplicate the winds at the lowest pressure available.

### 2.3 Population density data

The Gridded Population of the World (GPW) dataset (SEDAC, 2017) was used as a proxy for the urban component. GPW data are on 0.042 degree (2.5 arc-minute) grid and consists of estimates of human population density (number of persons per square kilometre) based on counts consistent with national censuses and population registers. When lower resolution data were required, they were obtained by averaging the original data within the new grid cells. Information about large city location and population, that was used to select cities for the analysis, was obtained from the World Cities Database available from <https://simplemaps.com/data/world-cities> (accessed on May 10, 2021).

### 2.4 Industrial point source locations

The algorithm of this study requires coordinates of industrial point sources as an input. In addition, emissions data from the U.S. and Canada are used to verify the emissions estimated from TROPOMI data. For the U.S., 2018-2020 point source NO<sub>x</sub> emissions from the U.S. Environmental Protection Agency (EPA) National Emissions Inventory (NEI) (EPA, 2020) based on a continuous emissions monitoring system (CEMS) are used. Note that the CEMS database is based on real emission measurements reported with 1-hour resolution that were then averaged over the analysed period. This database includes most of the sources including all large power plants. For sources that are not available from CEMS (e.g., oil refineries), emissions from eGRID database (<https://www.epa.gov/egrid/download-data>, accessed on August 5, 2021) for 2018 and 2019 were used. They are reported as annual emission estimates and we assume that the emission rates are the same throughout the year. This database includes emissions from oil refineries and cement factories that are often not available from CEMS. Finally, U.S. airport emissions are obtained from the 2017 NEI version released in January 2021 (<https://www.epa.gov/air-emissions-inventories/2017-national-emissions-inventory-nei-data>). For Canada, annual emissions from the Canadian National Pollutant Release Inventory (NPRI, 2020) are used. Only Canadian and U.S. sources with annual emissions greater than 0.5 kt of NO<sub>x</sub> per year were selected and used in this study.

Coordinates of the European industrial point sources were obtained from European Pollutant Release and Transfer Register (<https://prtr.eea.europa.eu/>) for 2007-2017 (accessed on March 2, 2021) and those that emitted more than 0.5 kt yr<sup>-1</sup> of NO<sub>x</sub> are included in the analysis. The world powerplant database (<https://globalenergymonitor.org/projects/global-coal-plant-tracker/>) was used to find locations of power plants for the global analysis. Missing sources were added based on the analysis of the NO<sub>2</sub> residuals maps (see Section 3) and then confirmed using satellite imagery as was previously done in other studies (e.g., McLinden et al., 2016; Fioletov et al., 2016; Dammers et al., 2019; Beirle et al., 2021). Satellite images from Google (<https://www.google.com/maps>), Microsoft Bing (<https://www.bing.com/maps>), and Sentinel 2 (<https://apps.sentinel-hub.com/eo-browser/>) maps were used for this purpose. Multiple image sources were used since some of the images from Google maps are not always up to date and may not show recently-build factories.

## 2.5 Elevation data

Elevation data were one of the proxies used in the statistical model. Elevation data used in this study are from 2-Minute Gridded Global Relief Data (ETOPO2v2) database (NOAA, 2006). When lower resolution data were required, they were obtained by averaging the original data within the new grid cells.

## 5 2.6 Google mobility data and analyzed period

The lockdown periods due to the COVID restrictions varied from country to country, but in most countries, they started in the second half of March 2020. In the analysed Canadian cities, the lockdown started between March 12 and 17. In the U.S., it started between March 18-19 (Atlanta, Los Angeles) and April 2 (Houston). In Europe, the lockdown started as early as on March 8 (Milan), but for most of the cities the lockdown was introduced after March 14. The second half of March is also the time when the lockdown measures started in many other cities around the world including Auckland, Baghdad, Buenos Aires, Johannesburg, Lagos, Manila, New Delhi, Sydney, and many others (Levelt et al., 2021, their Appendix B).

It is more difficult to determine the time of return to normal activities because the restrictions were often lifted in phases. For example, in the U.S., a “stay at home” order was lifted between April 30 (Texas) and June 11 (New Hampshire). Moreover, there was no formal lockdown in some countries (Belarus, Japan, South Korea, Sweden, Taiwan), but a decline in public activities can be seen even in these countries as well. For example, there was up to 40% decline in road transport emissions in Sweden even in absence of any formal lockdowns (Guevara et al., 2021). For this reason, we use mobility data as a proxy instead on the lockdown dates to select the analysed period.

The Google Community Mobility Report data (available from <https://www.google.com/covid19/mobility/>, accessed on March 1, 2021) were used to determine a common time period for our analysis. These data represent the changes in the number of people at locations of various types compared to a baseline level. A baseline day represents a normal value for that day of the week. The baseline day is the median value from the 5-week period Jan 3 – Feb 6, 2020. These mobility data can be used as a proxy for the urban traffic (e.g., Guevara, 2021) and are known to be correlated with urban NO<sub>x</sub> emissions (Venter et al., 2020; Bar et al., 2021; Misra et al., 2021). In this study, they were compared to urban and background NO<sub>2</sub> levels in different countries. The mobility data are available for several categories. Results for mobility for “retail and recreation” are presented as this category demonstrated the highest correlation with estimated urban emissions. The “retail and recreation” category covers visits to restaurants, cafes, shopping centres, theme parks, museums, libraries, movie theatres, and similar locations. We will refer to this category as to the “Google mobility data” for brevity.

Fig. 2 shows changes in Google mobility data (available as deviations relative to the baseline period) for the regions analysed in this study (see Section 4). During the three month-long period from March 16 to June 15, 2020, the mobility data were below the baseline level in all analysed regions. Note that for China, Google mobility data are not available, and the lockdown there occurred earlier (in February) except for Wuhan, where the lockdown was lifted on April 8. Note that there

was no formal lockdown in the Japan, South Korea, and Taiwan region, although we still see some decline in mobility data there.

### 3 The fitting algorithms

The technique used here is a further development of a point source emission estimation algorithm (Fioletov et al., 2015, 2016; McLinden et al., 2016; Dammeres et al., 2019) that was later expanded to estimate multi-source and area-source emissions (Fioletov et al., 2017, McLinden et al., 2020). This section provides only a general description of the method. The calculation formulas are given in the Appendix. The approach used in this study is based on a linear regression model. All satellite measurements over a certain area during a certain period are linked to locations of industrial point sources as well as to population density and elevation-related proxies by a few parameters that characterise these links. Thus, information from thousands of satellite measurements is compressed into a handful of parameters and therefore their estimates can have very low statistical uncertainties. Then, satellite measurements can be reconstructed using the regression model and contribution of three terms of the model (industrial, urban and background) can be studied. Such a model may not be very accurate in “predicting” values of individual satellite pixels, but we will show that it performs well when it is used to describe a three-month mean NO<sub>2</sub> VCD distribution over the analysed areas.

The method is adapted from the previously designed algorithm for multi-sources SO<sub>2</sub> emission estimates (Fioletov et al., 2017) where the emissions are determined from the best fit of satellite observation by a set of plume functions (one per source) scaled by parameters of estimation representing the emission strength. Unlike SO<sub>2</sub>, where emissions are mostly generated by point sources, NO<sub>2</sub> emissions also originate from area sources such as large cities. As shown in Fig.1, landscape also has a major impact on the NO<sub>2</sub> distribution. To accommodate these features, the statistical model was modified to:

$$TROPOMI\ NO_2 = \alpha_0 + (\beta_0 + \beta_1(\theta - \theta_0) + \beta_2(\varphi - \varphi_0)) \cdot \exp(-H/H_0) + \alpha_p \Omega_p + \sum \alpha_i \Omega_i + \varepsilon \quad (1)$$

where  $\alpha_0$ ,  $\alpha_e$ ,  $\alpha_p$ ,  $\alpha_i$ ,  $\beta_0$ ,  $\beta_1$ , and  $\beta_2$  are the unknown regression parameters representing population density-related proxies and emissions from individual point sources and a background with contribution from the elevation;  $\Omega_p$  is the source plume function for the population density-related distributed source (or area source);  $\Omega_i$  are the source plume functions for industrial point sources;  $H$  is the elevation above sea level and the empirical scaling factor  $H_0=1.0$  km was introduced to make the exponential argument dimensionless and to account for altitudinal dependence better; and  $\varepsilon$  is the residual noise.

Eq.1 is a linear regression statistical model with unknown coefficient sets  $\alpha$  and  $\beta$ . There are three main components in the model: the background term,  $\alpha_0 + (\beta_0 + \beta_1(\theta - \theta_0) + \beta_2(\varphi - \varphi_0)) \cdot \exp(-H/H_0)$ , related to background and elevation (four fitted coefficients), the urban component term,  $\alpha_p \Omega_p$ , related to the population density (one coefficient), and the industrial term,  $\sum \alpha_i \Omega_i$ , that represents the contribution from industrial point sources (variable number of coefficients from zero to few dozens). We will refer to them as to background, urban and industrial components.



The fitting was done for all satellite pixels centered within 3° by 4° areas around large cities and collected during a three-month period by minimization of the squares of the residuals ( $\epsilon$ ). The size of the area is based on the following considerations: The larger the area the less accurate assumptions about a linear gradient of background NO<sub>2</sub> and constant emissions per capita are. The algorithm is based on fitting plumes. For typical plume characteristics (discussed below), the size of fitting area should be long, in order of 100 km, to have enough data for the fit. Finally, the area should be large enough to avoid correlation between the elevation and population density proxies.

As in Fioletov et al., (2017), the plume from an industrial point source  $i$  is described by a plume function  $\Omega(\theta, \varphi, \omega, s, \theta_i, \varphi_i)$  where  $\theta$  and  $\varphi$  are the satellite pixel coordinates;  $\omega$  and  $s$  are the wind direction and speed for that pixel; and  $\theta_i$  and  $\varphi_i$  are the source coordinates. An unknown parameter ( $\alpha_i$ ) represents the total NO<sub>2</sub> mass emitted from the source  $i$ . The emission rate for source  $i$  can be expressed as  $E_i = \alpha_i / \tau$ , where  $\tau$  is a prescribed NO<sub>2</sub> lifetime (or, more accurately, decay time, but we use the term “lifetime” because it is more common). Note that  $\tau$  is different from the chemical lifetime (de Foy et al., 2015). Once the emission rate is established, it can be used to reconstruct how distribution of NO<sub>2</sub> emitted by that source would be seen by a satellite, i.e., estimate the industrial component in satellite data. We expressed emissions rates in kt y<sup>-1</sup> in this study to make it easier to compare with the rates available from emissions inventories. However, all emissions calculations here are done for a 3-month period (from March 16 to June 15).

The plume functions  $\Omega$  are EMG functions that are commonly used to approximate plumes of VCDs of trace gases such as NO<sub>2</sub>, SO<sub>2</sub>, and ammonia (Beirle et al., 2011, 2014; Damers et al., 2019; Fioletov et al., 2017, 2015; de Foy et al., 2015; Liu et al., 2016; McLinden et al., 2020). Similar in concept to a Gaussian plume function, they also take into account the finite physical size of the source and the spatial resolution of the satellite instrument being utilized. The lifetime  $\tau$  reflects the rate at which NO<sub>2</sub> is removed from the plume due to chemical conversion or physical removal such as deposition; it depends on several factors such as season and NO<sub>2</sub> concentration. It is about 2-6 hours in summer and longer in winter (de Foy et al., 2014; Liu et al., 2016). Moreover, for some sources, the lifetime may be changing over time (Laughner and Cohen, 2019) as NO<sub>2</sub> concentration declines, although other studies suggest that such changes are minor (Stavrakou et al., 2020). Recent TROPOMI-based estimates show that a typical lifetime in urban areas is between 2 and 5 hours in spring and autumn with shorter lifetimes at low latitudes (Lange et al., 2021). While the lifetime has a large impact on the emission estimates, relative changes are less sensitive to it. In addition to  $\tau$ , the shape of the EMG function depends on the prescribed plume width ( $w$ ), that depends on the size of the source and the size of satellite pixel. The value of  $w=8$  km for plume width was used in this study for TROPOMI along with a constant value of  $\tau=3.3$  hours. These values are based on a sensitivity study where TROPOMI data over the Canada and U.S. were fitted by plume functions with various combinations of  $w$  and  $\tau$ . The switch from 7 to 5.6 km along-track resolution in 2019 might have some impact on the optimal plume width, but the sensitivity analysis shows that small changes in  $w$  have only a minor impact on the results. We estimated that, for the urban component, on average, a 1-hour deviation from the used  $\tau$  value (3.33 hour) or a 2 km variation in  $w$  changes the differences between 2020 and 2018-2019 values only by about 1%.

Unlike many previous studies (Beirle et al., 2011; Fioletov et al., 2016; Lange et al., 2021) where the background offset was presumed to be constant and estimated from, for example, upwind NO<sub>2</sub> data, we included a special term that is responsible for it. In equation (1), the  $\alpha_0 + (\beta_0 + \beta_1(\theta - \theta_0) + \beta_2(\varphi - \varphi_0)) \cdot \exp(-H/H_0)$  term is assumed to be declining exponentially with elevation, i.e., within the analyzed 3° by 4° area, the higher is the elevation the lower the background tropospheric NO<sub>2</sub> VCD is. It was also assumed that this contribution from elevation depends on geographical coordinates only and not on the winds. Even in absence of any sources, there could be some gradient in tropospheric NO<sub>2</sub> over the analyzed area, as for example, over some regions in northern Canada or along the east coast of the U.S. (Fig. 1). To account for such gradients, the linear term  $\beta_1(\theta - \theta_0) + \beta_2(\varphi - \varphi_0)$ , where  $\theta_0$  and  $\varphi_0$  are the coordinates of the centre of the analyzed area, was added. In other words, it was assumed that there is a linear gradient of background NO<sub>2</sub> within the analyzed area and NO<sub>2</sub> VCD declines exponentially with height over elevated regions. Finally,  $\alpha_0$  was added to the model to account for remaining free-tropospheric NO<sub>2</sub> at high elevations where  $\exp(-H/H_0)$  is very close to 0. Its presence gives a better agreement of the fitting results with the satellite data for areas with a high range of elevations. Since this term is a part of the statistical model, all parameters  $\alpha_0$ ,  $\beta_0$ ,  $\beta_1$ , and  $\beta_2$  are estimated from the fitting. Once they are estimated, the term can be calculated for any place within the analysed 3°×4° area that gives a “background” value for that location that depends on the coordinates and elevation only. For simplicity, we will refer to the term discussed in this paragraph as to the “background” component.

Finally, the  $a_p \mathcal{Q}_p$  term represents the emissions contribution from factors, related to urban activity. Such emissions can be estimated by establishing a regular grid and then estimating emissions for each grid point as was previously done for SO<sub>2</sub> (Fioletov et al., 2017, McLinden et al., 2020). If, for example, we use a 0.2° by 0.2° grid (i.e., 336 (16 x 21) grid cells) within the analyzed 3° by 4° area, this would mean that we need to add 336 unknown coefficients to Eq.1. It would make the coefficient estimates less robust and prevent us from estimating emissions from individual industrial point sources because their plume functions would be highly correlated with the plume functions of the neighboring grid cells. Instead, we assumed that emissions from each grid cell are proportional to the cell population and the coefficient of proportionality is the same for the entire analysed 3° by 4° area. Thus, we just need to estimate one coefficient ( $a_p$ ) that is proportional annual emissions per capita. This makes the statistical uncertainty of such coefficient very small. In fact, for most analyzed areas, the uncertainty were at least 10 times less than the coefficient itself. The composite plume function  $\mathcal{Q}_p$  is a sum of plume functions of all individual cell centres multiplied by the grid cell population. Thus,  $\mathcal{Q}_p$  depends on geographical coordinates, population density and local winds. The original population density data were converted to a 0.2° by 0.2° grid by averaging population density data within each grid cell. Smaller grids such as 0.1° by 0.1° were also considered, but it was found that the reduction of the grid size does not change the results, while increase the computation time.

The downside of this approach is that the estimates would produce mean emissions per capita for a rather large area. This may not be very representative if there are cities with different economical conditions within the analyzed area as, for example, at the border of North and South Korea. Such cases are easily identifiable from the maps of the fitting residuals: such cities would appear as areas of large positive and negative anomalies. We did find several such cases and manually adjusted the area to include only one highly populated area.

The proxy plume functions used in the model preferably should be uncorrelated, because otherwise the coefficients have correlated errors making their interpretation difficult. For a typical urban area, the plume functions related to urban activity and to industrial sources are expected to be independent: high population density zones typically occupy a small part of the area and industrial sources are typically located away from such highly populated zones. Note that the NO<sub>2</sub> lifetime is relatively short and the median wind speed in, for example, the eastern U.S. is about 10 km per hour, so sources located 30-40 km apart typically have uncorrelated plume functions.

High correlation between the population and landscape-related proxies is possible if a city is in a valley surrounded by mountains. The correlation could be reduced by increasing the size of the analysed area, but if the area is too large, the assumption that the background level has a linear gradient in the area may not be valid. Therefore, we limited the area to 3° by 4°. The correlation coefficients between the site elevation and population density for 3° by 4° areas are typically small. For example, in the U.S., correlations are positive over Florida (about 0.2) with the population density is higher in the inland area, and negative in the Portland-Seattle-Vancouver area (about -0.35), where it is higher near the ocean and lower in the mountains. As the plume functions of individual industrial sources are very local (~50 km footprint), they do not correlate with the elevation. With such low correlation coefficients, elevation does not affect estimates of other parameters of the regression model.

When industrial point sources are located in close proximity, their plume functions in the statistical model (Eq.1) are highly correlated. In practice, it often appears if, for example, estimated emissions from one source are unrealistically high, while emissions from the other near-by source are low or even negative. In such cases, emissions from individual industrial sources often cannot be estimated. However, the sources can be grouped into independent clusters and total emissions from such clusters can be estimated. Such grouping could be done manually on a case-by-case basis, but it would be subjective and very time consuming. Instead, we applied an algorithm based on factor analysis. We would like to emphasize, that the factor analysis, described in the next two paragraphs, was used to improve emissions estimation for individual sources or clusters of sources. It is not required if only total emissions from all point sources in the area are estimated in order to separate them from urban emissions or if all industrial sources are isolated remote sources.

To group industrial sources into clusters, an orthogonalization process was applied to the plume functions of individual industrial sources. First, the correlation matrix for the plume functions of individual point sources ( $\Omega_i$ ) was calculated and eigenvalues and eigenvectors (or “factors”) of the correlation matrix were determined. The correlation matrix was calculated just once using March 16 – June 15 data from all three years. An isolated remote source would appear as an eigenvector with an eigenvalue of 1. Two (or more) closely located, but isolated from others, sources, would have one corresponding eigenvector and an eigenvalue of 2 (or more). Eigenvalues lower than 1 mean that the corresponding sources are already partially included in other eigenvectors. To reduce the number of “factors”, only “factors” with eigenvalues > 0.6 were kept.

The approach based on eigenvalues of the correlation matrix creates proxies that are not correlated and reduces the number of the fitting coefficients. While they correctly describe the total contribution of all industrial sources in the area in the

total NO<sub>2</sub> variability (or total emissions), individual eigenvectors, i.e., linear combinations of the original plume functions, may not have clear interpretation. For example, they may include the original plume functions with negative coefficients. In order to avoid that and obtain proxies that have a meaningful interpretation, the eigenvectors were linearly transformed, so they became as close to the original plume functions as possible, while the correlation coefficients between them remained low. This was done using the varimax factor analysis method that is implemented in modern statistical software packages such as R and SAS (Belhekar, 2013). It orthogonally rotates the established “factors” to maximize the sum of squared correlations between the original variables and factors. Then, the algorithm uses a linear combination of the original variables that have the highest correlations with the rotated “factors”. I.e., the condition of orthogonality is removed in order to find the simplest linear combination of the original variables. In practice, the algorithm produces a set of “clusters”, i.e., linear combinations of the original plume functions, that have low correlation coefficients (typically less than 0.2) between them, and each cluster has high correlation coefficient (typically more than 0.95) with one orthogonal “factor”. To simplify this further, if a linear combination has a weight for an original variable under 0.2, its weight was set to 0. As a result, all non-isolated point sources were grouped into small clusters and emissions estimates were done for such clusters instead of individual sources, while each isolated remote source forms a single-source cluster that corresponds to only that source. It is possible that a single source contributes to more than one cluster that makes interpretation of emissions for such clusters more difficult, but such cases are rare.

As in any regression analysis-based study, correlation between the proxies is one of the main obstacles in the result interpretation. The “orthogonalization” of plume functions from industrial sources largely reduces cross-correlations between the proxies, but high correlations between industrial and population density-related plume functions are still possible if industrial sources are located in highly populated areas. In such cases, it may be difficult to separate its signal from the contribution of the population density-related proxy. For example, in one case (Edmonton, Canada) this correlation coefficient was as high as 0.94 and it was not possible to separate urban and industrial emissions. Without such separation, industrial emissions are counted as population density-related that makes Edmonton annual per capita emissions nearly twice as large than emissions for other cities. Note that for large cities and small industrial sources, high correlation means that the emissions from such industrial sources cannot be reliably estimated, although the impact on estimation of the population density-related signal is small. For this reason, industrial point sources located in the 0.2° by 0.2° cells where the population is greater than 600,000 people were excluded. This is an empirically estimated limit, and, in a few cases of very large cities (New York, Moscow), it was manually adjusted.

The fitting and parameter estimation was done using all individual TROPOMI level 2 pixels for the period from March 16 to June 15 four times: for 2018, 2019, 2020 and 2021. So, four sets of coefficients (one set per year) were obtained and then used to estimate the background levels and emissions. Then, the results for 2018 and 2019 were compared with these for 2020. We also performed the same analysis for 2021, but these results were only used to analyze interannual variability because COVID-19 lockdowns may still have some impact on NO<sub>2</sub> in 2021.

As the regression model has three main terms (background, urban and industrial), the NO<sub>2</sub> VCD for each TROPOMI pixel is represented in Eq. 1 as a sum of three values (components) plus a residual error. Then the values of individual components and residuals can be analyzed the same way as the original TROPOMI measurements, e.g., mean values over a certain period (in our case, March 16– June 15) can be calculated as a function of latitude and longitude.

This is illustrated in Fig. 3, where individual terms of Eq. 1 are shown for an area centered on Montreal. The area includes two large cities, Montreal (4.2 million) and Ottawa (1.4 million, including the sister city of Gatineau). The terrain elevations in the analysed area are in the range from just a few metres above sea level along the Saint Lawrence River to more than 500 meters 100 km north of Montreal. For this plot (as well as for Fig. 1 and other figures), we used a non-linear scale that is more sensitive to small quantities in order to make small deviations more pronounced. The top row of Fig. 3 shows the mean TROPOMI NO<sub>2</sub> data (Fig. 3a), the fitting results (Fig. 3b), and the difference between them or the residuals (Fig. 3c). The background, urban, and industrial components are shown in Fig 3 panels d, e, and f respectively.

The contribution of industrial point sources ( $\sum \alpha_i \mathcal{Q}_i$ ) is illustrated by Fig. 3 g-i. In the case of Montreal, total emissions from industrial sources are relatively small, less than 1.8 kt y<sup>-1</sup> from our estimates. Note that unlike the previous algorithm (Fioletov et al., 2017), where  $\mathcal{Q}_i$  represented plume functions from individual sources, this new  $\mathcal{Q}_i$  represents plume functions of clusters of closely located individual sources determined by factor analysis. The estimated parameter  $\alpha_i$  represents total NO<sub>2</sub> mass of the entire cluster, while  $\mathcal{Q}_i$  is a weighted sum of plume functions of individual sources in the cluster. The weighting coefficients are determined by the varimax technique, described above. In the case of Fig. 3, the first cluster is comprised of two sources and the second and third clusters are each just single point sources. The estimated parameter  $\alpha_i$  represents emissions from the entire cluster, required that  $\alpha_i \geq 0$ .

The background and urban component maps have a simple interpretation. Figures 3 j and k shows maps of the elevation and population density respectively. Not surprisingly, the background component, that is dominated by scaled elevation, looks similar to the elevation map itself. The urban component is the population density map convoluted with EMG functions and therefore it looks like a smoothed population density map.

The suggested algorithm essentially finds the emissions levels that give the best agreement with the TROPOMI data NO<sub>2</sub> VCD and then uses these estimates to “reconstruct” the spatial NO<sub>2</sub> distribution as well as contribution from each source. As explained by Fioletov et al., (2017), the technique of satellite VCD reconstruction from fitted coefficients  $\alpha_i$  using Eq.1 to isolate different components, can be applied to the reported emissions  $E_i$  by using  $\alpha_i = E_i \cdot \tau$ . This produces a map of VCD that would be seen by satellites if these reported emissions are the only sources of NO<sub>2</sub>. The same approach was employed here using U.S. emissions inventories. For such estimates, the ratio between NO<sub>x</sub> and NO<sub>2</sub> is required. Beirle et al., (2021, their Fig. 2), has recently estimated the NO<sub>x</sub> to NO<sub>2</sub> ratio for different parts of the world and found that the ratio is about 1.4 over the U.S. and typically between 1.2 and 1.6. elsewhere. The value of 1.4 was used in this study.

The quality of a regression model (Eq. 1) can be described in terms of the correlation coefficient between the original and predicted values. In case of Montreal, the correlation coefficient of about 0.55. I.e., a set of about half of million original TROPOMI observations over the 3° by 4° area during a three-month period can be described by just 8 parameters ( $\alpha_p, \alpha_0, \beta_0$ ,

$\beta_1$ , and  $\beta_2$  plus 3 coefficients  $\alpha_i$  for industrial sources) with that correlation coefficient. The model can be further improved by adding parameters responsible for weekday- weekend differences, seasonal changes, and meteorological proxies (Goldberg et al., 2021; Kim et al., 2021). However, we focused on the mean NO<sub>2</sub> changes over a 3-months period, and they can be successfully estimated without such additional parameters. Fig. 3 shows that the fitting results are able to reproduce such mean data accurately: in the case of Montreal, the coefficient of determination ( $R^2$ ), i.e., the ratio of the variance of the residuals (Fig. 3 c) to the variance of the averaged TROPOMI data (Fig.3 a) is between 0.9 (in 2019) to 0.93 (in 2020) meaning that fitting results “explain” from 90% to 93% of the observed variance. The Pearson correlation coefficient between the mean TROPOMI data and the fitting results is about 0.96 (Fig. 3 l).

The necessity of both linear gradient- and elevation-related components in the background term in Eq.1 is illustrated by Fig. 4. If the surface is nearly flat in the analysed area (as, for example, in the case of Minneapolis, Fig. 4 g), the background component is dominated by the linear gradient. However, the elevation affects the NO<sub>2</sub> distribution near mountain areas as, for example, in case of Seattle, where mountains as high as 2000 m are located east of the city (Fig. 4 i). It is interesting to note that the background components are practically identical for both periods that gives a high confidence in the obtained results. The influence of the landscape on the NO<sub>2</sub> distribution also explains why the distribution near Seattle does not look like a “hotspot” NO<sub>2</sub> distribution near a typical large urban area. As Fig. 4 shows, the statistical model can successfully reproduce the NO<sub>2</sub> VCD distribution in both areas. The Pearson correlation coefficient between the 3-month mean TROPOMI data and the fitting results for Minneapolis and Seattle are 0.96 and 0.94 respectively.

Since the fitting results are based on just a handful parameters, the approach of this study is to investigate changes in these parameters or the three regression terms themselves between 2020 and 2018-2019.

## 4 NO<sub>2</sub> VCD estimation results for urban areas

To test the method, the described technique was applied to the 22 largest urban areas in the U.S. and 5 in Canada (Fig. 5). Four examples with detailed analysis of the components of the NO<sub>2</sub> distribution are discussed below with results shown in Fig. 6. Eight types of maps are shown. They include mean values for the analysed period for the actual TROPOMI data (column *a*), the fitting results (*b*), the residuals (*c*), i.e., (*a*) minus (*b*), as well as individual components of the fitting: the background (*d*) and urban (*e*) components, and the industrial source clusters (*f*). The Fig. 6 is divided in 4 sections with the area name shown on the top of each cluster of plots.

As mentioned in Section 3, reported emissions can be used to “reconstruct” VCD distribution for NO<sub>2</sub> emitted from these sources using Eq.1. The maps of NO<sub>2</sub> VCDs from the reported bottom-up emissions is shown in Fig. 6 (column *g*). We would like to emphasise that such reconstruction is based on industrial emissions data only, without any satellite NO<sub>2</sub> observations (although  $\tau$  and  $w$  in the plume functions were the same as in the satellite-based estimates). Finally, the maps of the difference between TROPOMI industrial sources-related component (Fig. 6, column *f*) and NO<sub>2</sub> VCD from reported “bottom-up” emission-based reconstruction (Fig. 6, column *g*) is also shown in Fig. 6 (column *h*).

## 4.1 Case studies

Four examples that represent different cases of NO<sub>2</sub> distributions around large urban areas are discussed below. In the case of Boston, there is a single urban source with no large industrial sources nearby and with relatively small impact from the terrain. The Atlanta area represents the case where the urban component is well-separated from industrial sources and the area also contains the world largest airport. In the Pittsburgh area, industrial and urban sources have comparable contributions, and the TROPOMI-based industrial emissions estimates can be validated by EPA NEI CEMS measured emissions. Multiple industrial sources in the Houston area are missing from the used EPA NEI CEMS emissions database and in this example emissions from the EPA eGRID database can be compared with TROPOMI-based estimates.

Boston is a major urban area with a population of more than 8 million (for the Combined statistical area of Greater Boston). On the TROPOMI NO<sub>2</sub> map (Fig. 6, column *a*), it appears as a large “hotspot” that can be successfully reproduced by the statistical model (Eq.1) using the population density as a proxy. From our estimates, there is a  $-24\% \pm 2\%$  decline (the error bars correspond to 2- $\sigma$  for random uncertainty, see Section 4.3) in the urban emissions in 2020 compared to the 2018-2019 average. Our estimates of urban emissions changes in 2020 are similar to the -22.8% drop in TROPOMI NO<sub>2</sub> values estimated by Goldberg et al., (2020) for the period from March 15 to April 30; and -18.3% drop estimated by Bar et al., (2021) for the period from March 22 to May 30. Boston also shows one of the largest in the U.S. declines in the background component (about  $20\% \pm 0.5\%$ ). Although the background component is not linked to particular plumes, it is likely that very high emissions from the largest in the U.S. NO<sub>2</sub> hotspot over the New York-Philadelphia contributed to the background NO<sub>2</sub> over Boston and decline in emissions there caused changes in the background NO<sub>2</sub> over Boston.

Our estimate of the urban emissions decline for Atlanta is about  $-35\% \pm 2\%$ . This is higher than the -20% decline estimated by Goldberg et al., (2020). However, changes in the background component where about  $-13\% \pm 0.4\%$ , while the background (Fig. 6, column *d*) component over Atlanta is comparable to the urban (Fig. 6, column *e*) component (both are about 0.04 DU), so decline of the sum of the two components over Atlanta should be about -23%. The urban component estimates are based on fitting of the plume from the city itself where NO<sub>2</sub> is dominated by on-road vehicle emissions. Kondragunta et al., (2021) estimated that the decline in on-road emissions is about -28%, that is closer to our estimate. The Atlanta area also hosts the Hartsfield–Jackson Atlanta International Airport (labelled as “1” in Fig 6, column *h*), the world’s busiest airport with more than 100 million passengers per year in 2018-2019 (<https://aci.aero/data-centre/annual-traffic-data/passengers/2017-passenger-summary-annual-traffic-data/>). The Atlanta airport NO<sub>2</sub> signal can be easily isolated since the airport is located far away from industrial sources (the correlation coefficients between the plume functions are less than 0.2) and at a distance from Atlanta city’s most populated area (the correlation coefficient is 0.54). VCDs estimated for the industrial source clusters (column *f* in Fig. 6) are in line with those based on reported emissions (column *g* in Fig. 6). Our estimated annual emissions for the airport are  $5.1 \pm 0.2$ ,  $6.4 \pm 0.2$ ,  $2.9 \pm 0.2$  kt y<sup>-1</sup> in 2018, 2019, and 2020 respectively, while the EPA emissions inventory value is 3.7 kt y<sup>-1</sup> for 2017 (the last available year). Thus, our estimates show a 55% decline in airport emissions between 2019 and 2020. The decline in aircraft operations for the analysed period was about 75% for passenger

flights and 25% for cargo operations (according to Department of Aviation, Hartsfield-Jackson Atlanta International Airport, <https://www.atl.com/business-information/statistics/>, accessed on Nov. 15, 2021). For illustration purpose only, for Hartsfield-Jackson Atlanta International Airport, the 2017 EPA emissions inventory value was used to calculate NO<sub>2</sub> VCD in column *g* of Fig. 6 for 2018 and 2019 and a half of that value for 2020.

5           The Pittsburgh area includes the cities Pittsburgh (population of ~2.4 million) and Cleveland (~3.6 million) and has one of the highest emissions from industrial sources among the analysed areas. Several coal-burning power plants are located east, west, and south of the city. Their emissions are comparable or even larger than from Pittsburgh itself. The NO<sub>2</sub> distribution around major industrial sources “reconstructed” from the reported emissions (Fig.6, column *g*) is similar to the NO<sub>2</sub> distribution from industrial sources based on satellite estimates (Fig.6, column *f*). The differences (column *f* minus column *g*) are small  
10 although NO<sub>2</sub> from the reported emissions are slightly larger for the cluster of power plans east of the city. The total reported emissions from all industrial sources in the Pittsburgh area are 43, 37, 26 kt y<sup>-1</sup> for 2018, 2019, 2020 respectively, while our estimates are 36, 34, 24 kt y<sup>-1</sup> (with 2- $\sigma$  uncertainty of about 1.5 kt y<sup>-1</sup>), i.e., the 2020 decline from our estimates is 35%, while the decline in reported emissions is 31%. The urban emissions declined from about 72 $\pm$ 2.3 kt y<sup>-1</sup> in 2018 and 2019 to 36 $\pm$ 1.2 kt y<sup>-1</sup> in 2020, i.e., by -50%.

15           In the case of Houston, the EPA NEI CEMS emissions inventory contains emissions from the power plants in the area, but not from large oil refineries that are responsible for hotspots seen on the TROPOMI mean NO<sub>2</sub> plot. Their coordinates and emissions estimates were obtained from the eGRID inventory. The reported industrial emissions values for the analyzed Houston area in 2018-2019 are 17 kt y<sup>-1</sup>, while our estimates are 36 and 31 kt y<sup>-1</sup> for 2018 and 2019 respectively and the estimated value for 2020 is 33 kt y<sup>-1</sup>. It appears that TROPOMI-based emissions estimates agree with emissions from the  
20 power plants from CEMS but are noticeably larger than emissions from oil refineries available from the eGRID inventory (Fig. 6, column *h*). Our estimated changes in background and urban components for the Houston area are -2.3% $\pm$ 0.4% and -18% $\pm$ 1.6% respectively, i.e., we see a decline in the urban component and practically no changes in the two other components. Goldberg et al., (2020) estimated the decline over Houston in -15.6%, although the spread between three used methods of estimation is large, from -26.3% to -1.9%. Note that the lockdown period in Houston was relatively short, from April 2 to  
25 April 30.

## 4.2 Relative contribution of different components

NO<sub>2</sub> VCD represents total number of molecules, and equivalently mass, per area unit. When background, urban, and industrial components of the NO<sub>2</sub> distribution are estimated as described in Section 3, it is possible to calculate the total NO<sub>2</sub> mass, of each of the components and estimate their relative contribution to the total NO<sub>2</sub> mass. The diagram in Fig. 7 shows  
30 such contribution of individual components for the Montreal area (Fig. 3 *d, e, f*). Most NO<sub>2</sub> mass is associated with the term related to the background component. For the Montreal area, the contribution of industrial sources is four times less than the contribution of the urban component and the two of these components are responsible for less than a quarter of the total NO<sub>2</sub> mass in the area. Relative contribution of the three components in the other areas for the 2018-2019 period are shown in Fig.



S1. Most of NO<sub>2</sub> mass belongs to the background component that is not directly linked to plumes from urban and industrial sources. These plumes are responsible about a third of total satellite estimated NO<sub>2</sub> mass in New York and Los Angeles and far less in the other analysed 3° by 4° urban areas in the U.S and Canada. This result depends on a particular size of the area, but the fraction of the background component is larger for larger areas as all major urban areas are already included in the analysis. Fig. S1 also shows that NO<sub>2</sub> mass emitted from cities are larger than emissions from the industrial sources for most of analysed areas in the U.S. and Canada. Note that characteristics such as the mean background value and annual emissions per capita are much less dependent on the area size and the rest of the study is focused on them.

The mean NO<sub>2</sub> distribution near major emissions sources has sharp gradients that suggest that the NO<sub>2</sub> lifetime is relatively short, on the order of a few hours that is also confirmed by direct estimates (Beirle et al., 2011; de Foy et al., 2015). However, large background component may suggest that the lifetime should be relatively long since NO<sub>2</sub> distribution follows the terrain over large areas. This difference in the lifetime could be reconciled if we assume that a fraction of NO<sub>2</sub> emitted from cities and industrial sources gets into the free troposphere and have a longer lifetime there than near the ground. Also, levels of the OH radical, the main chemical NO<sub>x</sub> sink, within a plume can be much larger than under “clean” conditions and NO<sub>2</sub> lifetime could be longer under such condition than in the plume (Juncosa Calahorrano et al., 2021). Other sources, e.g., lightning or soil emissions may contribute to background component NO<sub>2</sub> directly. The background term can also include components of stratospheric NO<sub>2</sub> that was imperfectly removed as part of the retrieval algorithm (von Geffen et al., 2020). Finally, estimates of NO<sub>2</sub> lifetime from TROPOMI data (e.g., de Foy et al., 2015; Liu et al., 2016; Lange et al., 2021) are based on daytime observations only. However, the lifetime at night could be different (Kenagy et al., 2018) and nighttime emissions and NO<sub>x</sub> evolution during the nights are not reflected in our estimates.

### 4.3. Variability and uncertainty estimates

Two characteristics of uncertainties of the estimated NO<sub>2</sub> components are calculated, and the results are presented in Table 1. Uncertainties related to the random measurement errors can be estimated assuming that the residuals  $\varepsilon$  in Eq. 1 are uncorrelated and have the same variance. Since the total number of satellite pixels in the statistical model is very large, several hundred thousand, and the number of parameters is small, such uncertainties are typically low. These uncertainties are calculated for the three components in each analysed year and the average value for each area (in percent) are given in Table 1 as “random error”. On average, these random errors are about 0.25%, 1% and 3% for the baseline, urban, and industrial components respectively. The random uncertainty represents how precise the component value is calculated and provides the lowest limit of the total uncertainty.

Interannual variability is another characteristic that reflect uncertainties related to the contributions from meteorology, possible instrument or algorithm-related issues, differences in sampling due to variations in cloud cover, and perhaps, other factors. It is also affected by the changes in emissions themselves. Internal variability can be estimated by comparing the components, estimated for different years. The 2020 data are not used in this estimate since they were largely affected by the lockdowns. Instead, we added estimates for 2021 and calculated the standard deviations from the three values (Table 1).

Although estimates from just three data points are not very reliable, they show similar results for most of the analyzed areas and their average can be used as a characteristic of the interannual variability. The average standard deviation of the interannual variability for the background component is only 7.5%. The interannual variabilities for the urban and industrial components are 10% and 18% respectively. The interannual variability represents the upper limit of the total uncertainty.

The uncertainty of the percentage change between 2018-2019 and 2020 values is a combination of the uncertainty of the baseline, estimated from just two years and the uncertainty of the 2020 value. This gives the following values for 2- $\sigma$  confidence limits for the percent changes: 18%, 24%, and 44% for the baseline, urban, and industrial components respectively.

#### 4.4 The COVID-19 lockdown impact: the U.S. and Canada

The ability of the method to isolate individual components of the satellite measured total NO<sub>2</sub> mass makes it possible to estimate the impact of the COVID-19-related lockdown on these components separately. As mentioned, we compared the averages for the period from March 16 to June 15 in 2018 and 2019 to the same period averages for 2020.

To illustrate the changes in the background component, Fig. 8 (top) shows the mean VCD values of that component shown in Fig 6, column *d* (or, in other words, the mean value of  $\alpha_0 + (\beta_0 + \beta_1(\theta - \theta_0) + \beta_2(\varphi - \varphi_0)) \cdot \exp(-H/H_0)$ ) for the analyzed areas for the two time intervals (left column) as well as the percentage change in 2020 vs. 2018-2019 values (right column).

The mean value of decline for the background components among all urban areas is  $-6.5\% \pm 3.0\%$ . As mentioned, the largest decline of the background component was observed at Boston. The decline was also large, about -20%, over two areas (Edmonton and Calgary) in Canadian province of Alberta. It is unlikely that this decline is related to the lockdown: the restrictions in Alberta were not as tight as in many other areas: only some non-essential services were closed on March 27 and the restriction started to be eased in May (<https://edmonton.citynews.ca/2020/12/24/2020-look-back-albertas-pandemic-response/> accessed on Nov. 20, 2021). In 2020, Alberta had a “historically low” level of forest fires: by June of 2020, fires had burned just about 450 hectares of forest, compared to, for example, 650,000 hectares by June of 2019. (<https://globalnews.ca/news/7396849/alberta-2020-slow-wildfire-season/> accessed on Nov. 10, 2021) and therefore, likely lower than normal natural NO<sub>2</sub> emissions resulting in lower background levels.

The changes in the urban component are shown in Fig. 8 (middle row) expressed as annual NO<sub>2</sub> emissions per capita. Recall, that emission rate is the mass divided by the constant lifetime, therefore, the percent changes in emissions per capita and the changes in total mass are identical. The relative changes for the urban component (Fig. 8 right column) are typically larger than those for the background component. The average total emissions per capita declined by -28% in 2020 compared to 2018-2019 average (from 5.6 to 4.2 kg per year). The median value of decline among all urban areas is -26% and the mean value of percentage decline is  $-27\% \pm 6.2\%$ . The changes in emissions per capita are rather uniform except Vancouver where 2020 emissions are 15% larger than the average 2018-2019 emissions. This Vancouver anomaly is within the 2- $\sigma$  limits of natural variability as discussed in section 4.3 (Table 1) and may be related to unusual meteorology and persistent cloud cover there in 2020. Edmonton is excluded from this panel because two industrial sources are located in the city itself and, therefore, it is hard to separate their emissions from the urban emissions.

The number of sources and emission strength from large industrial sources varies from area to area. Some areas, e.g., Las Vegas, do not have such emissions sources at all. The total emissions from all large industrial emissions sources and percentage change in emissions are shown in Fig. 8 (bottom row). The mean value of percentage decline in the areas with industrial sources is  $-22\% \pm 1\%$ . Unlike background and urban components, changes in emissions from industrial point sources demonstrate rather large scattering from one area to another. It is not a surprise since in addition to the difference in the strength and length of the lockdown between the areas, there is a difference in the lockdown impact on various industrial sectors.

Overall, the 2020 values for the baseline and industrial components at individual sites are within  $2\text{-}\sigma$  limits of the interannual variability (the grey dashed lines in the right panel of Fig. 8) with just few exceptions, while 16 of 27 urban component values are outside these limits. As noted in Section 4.3, the interannual variability is rather large and therefore, the decline for individual areas is often not significant. For this reason, we analysed 27 individual areas covering a vast region with very different meteorological conditions, so the average of individual area estimates (i.e., the regional mean) can be calculated with high confidence. Indeed, the regionally mean values of the ratios of changes in 2020 urban and industrial components to the standard errors of these regional means are about 8.5 and 5.9 respectively (assuming that deviations for individual areas are not correlated), i.e., well outside the limits of interannual variability. The approach that is focused on regional statistics rather than on individual areas is used for all other regions in this study.

Since industrial point source emissions estimates are obtained as part of our TROPOMI  $\text{NO}_2$  VCD data analysis, such estimated emissions can be compared to the reported ones. In general, there is an agreement between estimated and reported emissions, as was already demonstrated in Fig. 6 a. The scatter plot of estimated vs. reported emissions in 2018-2019 is shown in Fig. 9 for the U.S. urban areas. Each dot on the plot corresponds to industrial emissions from one area in either 2018 or 2019 with the total of 40 data points. The correlation coefficients between the two data sets from Fig. 9 is 0.84. The slope of the regression line is about 0.7 suggesting that, on average, our estimates are 30% higher than reported emissions. The standard deviation of the residuals is about  $5 \text{ kt y}^{-1}$ . This value gives an approximate uncertainty for point source of  $\text{NO}_2$  emissions estimates for a 3-month period from TROPOMI data. As it is a direct comparison with the actual reported emissions, it includes all possible sources of errors. Then, the annual  $\text{NO}_2$  emissions are expected to be estimated with uncertainties of about  $2.5 \text{ kt y}^{-1}$  that is twice less than about  $5 \text{ kt y}^{-1}$  for  $\text{SO}_2$  emissions uncertainties (Theys et al., 2020).

#### 4.5 The COVID-19 lockdown impact: Europe

The described technique was applied to the European Union countries (plus non-members from former Yugoslavia) where detailed information about the industrial emissions sources is available. The analysis was also done for  $3^\circ$  by  $4^\circ$  areas around 36 largest European cities with population greater than 1 million plus some national capitals with population more than 500,000. Note, that to avoid double-counting, if more than one city located within an area, we used that area just once (e.g., Manchester and Birmingham are in one area).

The absolute and relative changes between 2018-2019 and 2020 for the three components are shown in Fig. 10 and Fig. 11. The NO<sub>2</sub> decline of the urban component was particularly large, more than 50%, for the countries in the most western part of the continent where the strictest lockdown measures were taken: France, Spain, and UK (Fig. 10). In contrast, the decline in the German, Czech and some other East European cities was only 20-25% (Fig. 11). For this reason, two sub-regions were formed for the analysis: Europe-1 (Italy, France, Spain, Portugal, Belgium, Ireland, and UK) and Europe-2 with all other countries. In general, the mean background values and estimated NO<sub>2</sub> emissions rates per capita in Europe are similar to those in the U.S. and Canada. However, relative changes are somewhat different.

In 2018-2019, the estimated annual emissions per capita for both European regions were very similar to those for the U.S. and Canada. In 2020, the urban component declined in almost every analysed area. The average declines for Europe-1 and Europe-2 regions were  $-54\% \pm 4\%$  and  $-13\% \pm 8\%$  respectively. This is in general agreement with total NO<sub>x</sub> emissions reduction for these two European sub-regions: -50% for Europe-1 countries (Italy, Spain, France) and -15% to -25% for Europe-2 countries (Germany, Sweden) with -85% of the total reduction attributable to on-road transport (Guevara et al., 2021). The decline in Europe-1 was rather uniform with all but one area demonstrating a decline of more than -40%. In contrast, only two areas demonstrated a -40% decline in Europe-2, while most of the areas had a decline under -20%. Two areas in Europe-2 (Budapest and Belgrade) demonstrated an increase in NO<sub>2</sub>. They are located 320 km apart and it is possible that relatively high NO<sub>2</sub> values there were caused by some specific meteorological conditions in spring of 2020: the NASA GEOS Composition Forecasting (GEOS-CF) simulations with constant anthropogenic emissions show a positive NO<sub>2</sub> anomaly over Hungary in April-May 2020 (Liu et al., 2020b).

As in the case of the U.S. and Canada, the mean background component in Europe shows a smaller decline than the urban component. On average, it was  $-5.9\% \pm 2\%$  and  $-11.5\% \pm 3\%$  lower in 2020 than in 2018-2019 for Europe-1 and Europe-2 regions respectively, but it was pretty consistent as almost all individual areas demonstrated a decline. Large decline in population-related emissions and relatively small decline in the background component for Europe-1 and the opposite for Europe-2 may create an impression that here is anticorrelation between the background level and population-related component, but it is not true. The large decline in average background for Europe-2 was caused by large negative background values for the Scandinavian countries in 2020 that also had large negative changes in the urban components. As discussed later in Section 4.6, there is no correlation between the changes in the background levels and urban component.

The emissions from industrial sources also demonstrated a decline, although the scattering of the values is large as the changes varied from country to country and from sector to sector. Guevara et al., (2021) estimated that the emissions decline in the energy industry was up to -30% in Italy, but under -5% in Sweden. The emissions decline from the manufacturing industry was smaller, from about -15% in Italy, Spain, France, UK to -5% in Germany and near zero in Sweden. Emissions from aviation were reduced by -90% in all European countries (Guevara et al., 2021). We estimated changes in emissions only for industrial sources that are located in the analysed areas around major cities and therefore do not represent the entire industrial emissions, but our estimates also show a difference between Europe-1 and Europe-2 regions: the average decline values  $-34\% \pm 10\%$  and  $-13\% \pm 16\%$ , respectively.

The uncertainty estimates are also in general similar to those for the U.S. and Canada: the random uncertainty is about 0.25% for the background component and 1% for the urban component. The interannual variability estimates are also similar for the background component (5.6%, 6.8% and 7.5% for Europe-1, Europe-2 and Canada-U.S. respectively). The interannual variability for the urban component for Europe-1 (12%) is also the same as that for the Canada-U.S. region, but higher (15%) for the Europe-2 region (Supplement, Tables S1 and S2). For Europe-1, the decline of the background component is within the 2- $\sigma$  level for all the areas and the decline of the urban component outside the 2- $\sigma$  level for all the areas. For Europe-2 however, the decline of the urban component is inside the natural variability limits. For the industrial component, the variability is high and the 2020 decline is within the 2- $\sigma$  level for most of the areas.

For illustration purposes, four areas are examined in greater detail in Fig. 12. The Manchester map (Fig. 12 top row) illustrates a large area of high population density in Central England with several power plants to the East. Recall, that the urban component is essentially the population density convoluted with EMG functions and the two large hotspots in the urban component corresponds to Manchester and Liverpool area to the north and Birmingham area at the south. Our TROPOMI data analysis shows a  $-40\% \pm 1.4\%$  decline in the urban component and about  $-18\% \pm 5.6\%$  decline from total emissions from the power plants. These numbers are close the reported by the UK Office of National Statistics decline in road traffic ( $-35\%$  and  $-50\%$  for April and May, respectively) and industrial activity ( $-20\%$ ) (Potts et al., 2021). The estimated decline in the urban component is very close to the  $-42\%$  decline in the surface  $\text{NO}_2$  concentrations reported by Lee et al., (2020). In contrast, the background component shows almost no change in 2020 compared to 2018-2019. For this reason, the total decline in TROPOMI  $\text{NO}_2$  VCD over Manchester ( $-27\%$  according Barré et al., 2021, and  $-32\%$  according to Potts et al., 2021) is smaller than our estimates for the urban component alone.

Paris is an example of a city that appears as a large, isolated urban source. The change between the two periods in the background component (Fig. 12, col. *d*) is about  $-10\% \pm 0.5\%$ , while the decline in the urban component (Fig. 12, col. *e*) is about  $-57\% \pm 1.5\%$  clearly seen on the plot. As in the other cases, this value of decline is larger than the decline from TROPOMI  $\text{NO}_2$  VCD data without separation of the two component and closer to the changes in  $\text{NO}_2$  surface concentrations. Estimated decline in TROPOMI  $\text{NO}_2$  VCDs over Paris was about  $-30\%$  (Bauwens et al., 2020; Barré et al., 2021), while the estimated decline in  $\text{NO}_2$  concentrations was  $-40\%$ - $50\%$  (Keller et al., 2021; Barré et al., 2021). The terrain does not play a major role in background component for the Paris area. There is some north-south gradient in the background component with higher values at the north-eastern corner of the area. The only relatively large industrial point source in the Paris area is Charles de Gaulle Airport which is evident on the 2018-2019 plot and practically disappeared on the 2020 plot. Our estimates show about 90% decline in  $\text{NO}_2$  emissions from 2018-2019 averages (from about  $6.1 \pm 2.2 \text{ kt y}^{-1}$  to  $0.5 \pm 0.2 \text{ kt y}^{-1}$ ) that is in line with more than  $-95\%$  decline in the passenger traffic of Charles de Gaulle Airport in April and May 2020 (<https://www.parisaeroport.fr/en/group/finance/investor-relations/traffic> accessed on Nov. 10, 2021).

Milan was one of the first European cities where some lockdown measures were imposed in late February and  $-40\%$  to  $-60\%$  reduction in  $\text{NO}_2$  concentrations was reported (Collivignarelli et al., 2020). Complex terrain affects the  $\text{NO}_2$  distribution creating large differences between VCD values over the mountains and valleys and also makes it more difficult to fit the

observations with the plume functions based on assumption of straight-line plumes resulting in relatively high residuals. The background component shows practically no difference between the two periods. The contribution from industrial point sources for that area is small. The urban component demonstrates a  $-53\% \pm 1.5\%$  decline in 2020 that is similar to other TROPOMI-based estimates for Milan:  $-38\% \pm 10\%$  (Bauwens et al., 2020) and about  $-50\%$  (Barré et al., 2021), while the estimated decline in surface  $\text{NO}_2$  concentrations was only slightly larger,  $-41\%$  (Keller et al., 2021) and about  $-52\%$  (Barré et al., 2021). Such small difference in the decline between VCDs and surface concentrations may be due to a relatively small contribution of the background component to the total VCD: it is just about one third of the urban component over Milan.

The maps for the Prague- Dresden area illustrate how changes in  $\text{NO}_2$  from industrial sources reflect differences in COVID-19 lockdown policies in Germany and Czech Republic. The decline in the urban component was only about  $-16\% \pm 3\%$ . In addition to Prague, that component also includes cities in East Germany (Dresden, Leipzig), but the changes over these cities and Prague are similar and close to  $-20\%$  (Barré et al., 2021). Otherwise, the difference would appear in the residuals (Fig. 12, column c). The main industrial sources in the Prague area are coal mines and coal-burning power plants in Czech Republic west of Prague near the German border and in Germany north of Prague, near the Polish border. In Czech Republic, the  $\text{NO}_2$  values of the industrial component remain unchanged, while the values over German industrial sources declined by a factor of 2. This is likely the result of different approaches to coal power industry in two countries. In the Czech case, power plants remained fully functioning and certain steps were taken to assure smooth operation and protect the workers: employees of power plants stayed on their job for longer periods, to avoid the risk of infection at home (EC, 2020). In Germany, the power generation from coal-burning plants was reduced by 60% (from 13.4 TWh to 5.6 TWh per month) in April-May 2020 compared to 2019 (<https://www.energy-charts.info/charts/energy/chart.htm?l=en&c=DE&year=2020> accessed on March 1, 2021). As a result, we see a large difference in  $\text{NO}_2$  VCDs from the power plants in two countries.

#### 4.6 The global COVID-19 lockdown impact

To evaluate the COVID-19 lockdown impact worldwide, the analysis described earlier in Section 4 was performed for 261 urban areas around the world. All cities with population greater than 1 million were considered. However, some of them, particularly in Africa, do not produce significant  $\text{NO}_2$  emissions that can be measured by TROPOMI over the three-month period selected for this study. Another obstacle is in Western Africa, where biomass burning made it difficult to estimate “background” levels as they were very different from year to year. Biomass burning areas appears as large anomalies on the maps of the residuals (such as shown in Fig. 3 c) making the standard deviations of the residuals much higher than at the other African cities. For this reason, several areas with population over a million in Western Africa were not included in the analysis. In case of China, there are too many cities with population over one million. We raised the limit for China and considered only cities with population greater than 6 million to keep the number of analysed areas similar to other regions.

The analysis algorithm requires coordinates of individual industrial sources in order to separate them from the urban component. The world power plant database (see section 2.3) was used to locate most of the power plants. Other sources were identified from hotspots on the  $\text{NO}_2$  residual maps as typically correspond to emission sources that are not included in the

original fitting. Coordinates of such sources are determined from high-resolution satellite imagery and added to the point source list and then the fitting process is repeated. A total of 357 such additional sources were identified. Most of them were cement and steel factories, and oil refineries. In addition, the world busiest airports were included as “industrial” emission sources. However, other sources, e.g., ship tracks or major highways may still be missing that may affect estimates for some areas. Some of these sources are identifiable in the residual maps and could be added to the statistical model in the future.

The map of the background and urban components for all 261 sites in 2018-2019 is shown in Fig. 13. The analysed period from mid-March to mid-June is close to spring in the Northern Hemisphere and autumn in the Southern Hemisphere, i.e. the seasons with very similar values of lifetime (Lange et al., 2021). Therefore, seasonal differences between the two hemispheres should be minimal, and maps of the main estimated components should well represent their global distribution. The highest background values are seen over East China and the northern part of Central Europe, while the lowest are mostly over South America and East Africa.

The urban component demonstrates the highest values are over Siberian region of Russia. They are likely related to additional NO<sub>x</sub> emissions due to heating there since the climatological temperatures there are relatively low in March-April compared to other regions. Another hotspot is Edmonton, but as mentioned, its high value is due to poor separation of urban and industrial sources there. Annual emissions per capita are also high over Middle East. However, in this region we found that the population density data in some areas including, for example, Riyadh, may not be reliable and emissions per capita may be overestimated. The population density maps there do not match Google map satellite images and other proxies such as night light data. This requires further investigation.

As Fig. 13 (bottom) shows, the lowest annual emissions per capita are in South America, Africa, and India (under 2 kg y<sup>-1</sup>). Although emissions per capita were calculated for each area independently and the population and industrial sources vary greatly from area to area, the per capita values are uniform: for example, almost all areas in India marked by green dots (0 to 2 kg y<sup>-1</sup>), most of European areas are orange (4 to 6 kg y<sup>-1</sup>), etc. This further gives a confidence in the obtained estimates. Fig. 13 shows NO<sub>2</sub> emissions based on the NO<sub>2</sub> total mass estimates and a fixed lifetime. These could be further converted to the NO<sub>x</sub> emissions by applying a conversion factor that typically varies from 1.2 to 1.4 (Beirle, et al., 2021).

Note that the urban NO<sub>2</sub> “footprints” of cities with the same population vary greatly from region to region with the highest values in Northern Eurasia and Australia, and the smallest in Africa and India. To illustrate these large differences, Fig. S2 shows the examples of NO<sub>2</sub> distribution near cities with population of about 5-6 million with very large (Saint Petersburg, Russia) and very small (Dar es Salaam, Tanzania) per capita emissions. The total mass of NO<sub>2</sub> per capita related to the urban component for Saint Petersburg was 40 times larger than for Dar es Salaam.

Fig. 14 shows the maps of percent changes for individual areas for the background and urban components. Relative changes of the background component are typically within ±15% and much smaller than in the urban component. One of the regions with large negative changes in the background component is Middle East. As mentioned, the population density data are not always accurate in that region and the background component may not be perfectly separated from the urban and industrial components. In contrast, the urban component demonstrates a much larger decline, particularly over Europe-1 and

India. Note the changes in the urban and background components are fairly independent: analysis of all 261 areas revealed that the correlation coefficient between them is -0.007.

The estimates for individual areas were then grouped into 13 large regions with 10-20 areas in each: the U.S. and Canada, Europe-1 and -2, China, India, South-East Asia (also includes Pakistan and Bangladesh), Japan with Taiwan and South Korea, Northern Eurasia (former USSR countries and Mongolia), Middle East, Africa, Australia and New Zealand, Central America, and South America. The regions are based on geographical location with similarities in economic development and reactions to the COVID-19 pandemic were also considered. Then, the average characteristics of the background, urban and industrial components were calculated for each region. Johannesburg (South Africa), and Pyongyang (North Korea) were not included in any particular region because their NO<sub>2</sub> emissions were very different from those from neighbouring countries and therefore may bias regional statistics.

The summary results for the regions are shown in Fig. 15. The regions in Fig. 15 are sorted by relative decline in the urban component (from smallest to largest). The regional changes were calculated as the average of percent changes for individual areas for that region. The uncertainty values in Fig. 15 are based on variation of the values for individual areas within the region. The background component has the smallest variability among the three components typically between 5% and 9%. The urban component variability is between 7% and 17% and the decline observed in the urban component for South America, Europe-1 and India is outside 3- $\sigma$  limits even for individual areas in these regions. The industrial component was added to separate emissions from large industrial sources in the urban areas from urban emissions themselves. Emissions from such industrial sources are typically similar or smaller than urban emissions and the variability of the industrial component (10%-30%) is similar or larger than that for the urban component.

China shows the smallest and not significant decline in the urban component over the analysed period as the main COVID-19 lockdown in China occurred earlier (in February). Most of the regions demonstrated statistically significant urban emissions decline within the range -18 to -28%. The decline was the largest, -36 to -52%, in three regions: Europe-1, South America and India. The map of the urban emissions changes (Fig.14, bottom) shows that the first two regions indeed contain countries with large decline of urban emissions. In case of India, a similar decline can be seen in neighbouring Pakistan and Bangladesh. In Africa, a decline is seen at the south and the north of the continent, while countries in West Africa mostly show no decline and even some increase probably due to a contribution from forest fires.

As mentioned in section 4.3, the industrial NO<sub>2</sub> component varies from area to area and from one type of NO<sub>2</sub> source to another, although there are some clear regional differences. Chinese cities demonstrated small changes in both urban and industrial components (-2.8% and +5% respectively) with one exception. Emissions from Wuhan, the city where the pandemic began, declined by more than -60%. Industrial emissions there also declined, but only by -30%. The background component shows no change there. A very strict Wuhan lockdown ended on April 8, 2020, but during that lockdown, NO<sub>2</sub> emissions in Wuhan declined -82% relative to the 2019 level (Ghahremanloo et al., 2021). That strict lockdown period lasted for less than one third of the analysed period, but apparently, it took some time for NO<sub>2</sub> emissions to return to the pre-lockdown levels.



It is more difficult to interpret changes in industrial source emissions because they are changing over time for various reasons that may require an investigation on a case-by-case basis. For example, the large uncertainties in the industrial emission changes for Central America in Fig. 15 are caused by doubling of emissions from power plants near Havana. This increase is likely caused by emissions from three powerships (power plants on ships) with total capacity of 184 MW, that started their operation in Port de Mariel near Havana in the second half of 2019 (<https://karpowership.com/en/project-cuba>, accessed Nov. 4, 2021). The largest regional industrial emissions decline was observed over Europe-1 and India, i.e., where also largest urban emissions decline was observed. It is likely the severe restrictions during the COVID-19 lockdown period there affected the industrial activity. However, on a larger scale, this link is not that obvious. Although the lockdown had impact on industrial sources, the correlation coefficient between changes in urban and industrial emissions among all analysed areas is -0.01.

As mentioned, statistical errors related to the fitting procedure are relatively small due to a very large number of satellite pixels used in the fit. For the urban component, they are between 1% and 10% for the cities analysed in this study. However, the year-to-year variability could be high. Table 2 summarizes the uncertainty for the 13 regions analysed in this study. It is similar to Table 1; however individual rows contain the averages of uncertainty estimates for all individual areas in the region. The uncertainties for the background component are between 4.9 and 9%. The urban component demonstrates the interannual variability between 9% and 22% with the largest value over the Middle East were, as mentioned, there could be a problem with the population density data quality. It is far more difficult to interpret the estimated interannual variability for the industrial sources because it depends on multiple factors from the meteorological conditions to the emission strength itself. The main conclusion here is that it is typically -10% to -20% for emissions from large (about 5 kt y<sup>-1</sup> or more) sources estimated based on 3 months of data.

To demonstrate that the observed NO<sub>2</sub> changes in urban emissions are indeed linked to the restricting measures taken by different countries, the estimated percent NO<sub>2</sub> changes in annual emissions per capita were compared to the Google Each Community Mobility Report data. The mobility data represent the changes in the number of people at locations of various type and can be used as a proxy for the urban traffic. The changes in the background and urban components were calculated for every country and compared to changes in mobility data. Only countries with two or more cities were used in the comparison. Note that the mobility data were averages of all regions for the entire country, while the NO<sub>2</sub> changes were estimated for areas around large cities only. Mobility data for China, Korea and some other countries were not available.

The scatter plot of the mobility and the NO<sub>2</sub> VCD changes (Fig. 16) demonstrates a very different relationship between the urban and background components. Changes in mobility and urban components are correlated (Fig. 16 left). As expected, the relative changes in the urban component are smaller than the mobility changes as the urban component includes more than just mobility-related traffic. The highest correlation is observed when changes in the NO<sub>2</sub> urban component are compared with mobility for “retail and recreation”, covering visits to restaurants, cafes, shopping centers, theme parks, museums, libraries, movie theatres, and similar locations. The correlation coefficient between the percent changes in per capita emissions and “retail and recreation” mobility is 0.62 (the probability that there is no correlation is less than 0.0003). There is no statistically significant correlation (the correlation coefficient is -0.08) between the background NO<sub>2</sub> and mobility data (Fig. 16 right).

For individual areas, the uncertainties due to the interannual variability rather large, so the observed 2020 decline of the urban component in many areas is within that uncertainty. Regional averages are more accurate and declines in urban emissions are statistically significant for all regions except China. Finally, mean 2020 declines of all areas (except China) are  $-6.0\% \pm 1.2\%$  and  $-26.7\% \pm 2.6\%$  for the background and urban components respectively that corresponds to 10- $\sigma$  and 20- $\sigma$  levels (Supplement, Fig. S3). In 2018, 2019, and 2021, such global averages are remarkable stable, as all mean values are within  $\pm 2.5\%$ , and within  $\pm 5\%$  if the means are taken with the two-sigma uncertainties. This suggests that there are no substantial drifts or shifts on the global scale in TROPOM data and the 2020 data is clearly an outlier.

## 5 Discussion and conclusion

Statistical regression analysis was used to separate contribution from industrial sources, urban areas, and background levels to the satellite observed tropospheric NO<sub>2</sub> columns (VCDs) and to study the impact of the COVID-19 lockdown on each component separately. The analysis was done for 261 major urban areas around the world grouped into 13 large regions. The algorithm also estimates urban and industrial emissions assuming a constant NO<sub>2</sub> lifetime (or, more accurately, decay time). A constant value of 3.3 hours was used as the lifetime.

To verify the obtained emissions estimates, we compared our result with the estimates from a similar study by Lange et al., (2021). In that study, TROPOMI NO<sub>2</sub> data were used to estimate emissions from 45 sources worldwide and then the results were compared with the available emissions inventories and some other satellite-based emission estimates. There were 33 sources common to both works. In order to compare them we first calculated our total emissions, i.e., the sum of urban and industrial emissions, and then converted them to the same lifetimes as in Lange et al., (2021), and then multiplied them by 1.4 to calculate NO<sub>x</sub> emission. As expected, our emission estimates were higher than from Lange et al., (2021) because there is typically more than one emissions source in the analysed 3° by 4° areas of this study. Nevertheless, there is 0.78 correlation coefficient between the two estimates.

Unlike other similar studies that simply removed the background offset (e.g., Beirle et al., (2011); Lange et al., (2021)), this study included the background component as a function of the elevation in the analysis. On a scale of several hundred km (as we analyzed 3° by 4° areas), most of the NO<sub>2</sub> mass is typically related to the background component. Even in the areas such as New York City, the background component accounts for 2/3 of the total mass. This explains why the estimated impact of the COVID-19 lockdown in urban areas depends on the size of the analysed area: the larger the area the more background NO<sub>2</sub> it includes and, therefore, the smaller the NO<sub>2</sub> difference between the COVID-19 lockdown and reference periods.

In most of the analysed areas, changes in the background components between the COVID-19 lockdown period analysed here (from March 16 to June 15, 2020) were typically within 10% from the 2018-2019 levels. In contrast, the urban component, based on population density, demonstrated a substantial and rather uniform decline of about -18% to -28% in most of the regions. Two regions (most western part of Europe and India) demonstrated a larger decline, about -40% to -50%. China

showed a much smaller decline ( $-4.4\% \pm 8\%$ ) because the lockdown there occurred prior to the analysed period. As for industrial point sources, emissions from them varied from region to region and from sector to sector. They demonstrate a decline of about -20% or less except for India and Europe-1 regions.

Abrupt changes in urban and industrial emissions due to COVID-19 lockdown did not immediately result in a similar decline in the background component. This may explain why large changes in NO<sub>2</sub> emissions in urban areas produced a relatively small, about 9% decline in global NO<sub>2</sub> (Bray et al., 2021). The importance of background NO<sub>2</sub> VCD was previously noted by Qu et al., (2021) and Silvern et al., (2019) when they found that the observed satellite tropospheric NO<sub>2</sub> VCD trends in remote areas do not match the expected changes. The origins of background NO<sub>2</sub> are still largely related to urban and industrial sources as it is clearly higher in the northern hemisphere, particularly over China, Central Europe and Eastern U.S., than in the southern hemisphere and tropics. However, the analysed three-month period may simply not be long enough for the lockdown to cause large changes in the background levels. There are also other NO<sub>x</sub> sources such as soil emissions (Hudman et al., 2012; Sha et al., 2021). They as well as sources aloft, such as lightning, and to a lesser extent, aircraft NO<sub>x</sub> directly contribute to the background component. It is estimated that lightning is responsible for roughly 16% of global production and most of this NO<sub>x</sub> is found in the free troposphere (Bucsela et al., 2019). Furthermore, Zhang et al., (2012) estimated that sources such as lightning, soils, and wildfires that account for about 20% of emissions annually and up to 39% in summer. Satellite measurements are also more sensitive to NO<sub>2</sub> in the free troposphere than in the boundary layer and relatively small amounts of NO<sub>2</sub> there produce a larger signal in satellite data. Another possible explanation is that at low NO<sub>2</sub> concentration in the boundary layer and free troposphere may have longer lifetimes than in the plumes. The fact that NO<sub>2</sub> fluctuations remain persistent over longer time in clean conditions than over polluted areas (Vinnikov et al., 2017) indirectly confirms that.

Barré et al., (2021), noticed a different lockdown-related decline between NO<sub>2</sub> VCDs and surface concentrations (-23% and -43% over Europe respectively). Moreover, Qu et al., (2021) reported that VCDs and surface concentrations had a similar decline between 2019 and 2020 at only 5% of the most pollutes sites. At the other sites, TROPOMI NO<sub>2</sub> VCDs data demonstrated, on average, a smaller decline than surface concentrations. Different changes in background and urban components in TROPOMI NO<sub>2</sub> could explain this inconsistency between the surface and satellite VCD-based results. The urban component is directly linked to city plumes and therefore is a better proxy for surface concentrations in polluted areas, while the background component includes contribution from other sources that were not affected by the lockdown.

The urban and industrial components are based on plume dispersion functions that correspond to NO<sub>2</sub> near the ground, almost always in the boundary layer. The urban component is based on the population density and the assumption that annual emissions per capita are uniform in the analysed 3° by 4° area. There are very large differences, up to factor of 40, in estimated emissions per capita among the different areas. The estimates were done for 3-month periods. For such a short time interval, most of the cities with population more than 1 million produce a statistically significant signal that can be readily detected in TROPOMI NO<sub>2</sub> data. As estimated emissions per capita are rather uniform, they can be used to account for urban component

outside large cities. Thus, it should be possible to estimate background, urban, and industrial components on the global scale and analyse the residuals in search of other factors contributing to the NO<sub>2</sub> budget.

The approach described in this study can be used to estimate emissions from cities and industrial point sources. For the latter, only source coordinates are required. A comparison of reported and TROPOMI-derived NO<sub>x</sub> emissions for the U.S. demonstrated a good correlation between them. As source coordinates can be also detected from satellite data alone (Beirle et al., 2019; Ding et al., 2020; McLinden et al., 2016), it may be possible to develop an independent “top-down” NO<sub>x</sub> emissions inventory from satellite measurements to complement and improve available “bottom-up” inventories as it was done for SO<sub>2</sub> (Liu et al., 2018). This could be important for regions, where no other emissions information is available.

### **Data availability**

The TROPOMI NO<sub>2</sub> product is publicly available on the Copernicus Sentinel-5P data hub (<https://s5phub.copernicus.eu>). The reprocessed (RPRO) and offline mode (OFFL) data of version V1.2.2 to version V1.3.2 were used. The Google Each Community Mobility Report data are available from <https://www.google.com/covid19/mobility/>. The Gridded Population of the World (GPW) dataset is available from NASA Socioeconomic Data and Applications Center at <https://sedac.ciesin.columbia.edu/data/collection/gpw-v4>. The European Centre for Medium-Range Weather Forecasts (ECMWF) ERA5 reanalysis data are available from <https://www.ecmwf.int/en/forecasts/datasets/reanalysis-datasets/era5>. Elevation data are from gridded global relief ETOPO2v2 database (<https://www.ngdc.noaa.gov/mgg/global/etopo2.html>).

### **Author contributions**

VF analysed the data and prepared the paper with input from CM and critical feedback from all the co-authors. CM and DG generated the TROPOMI data subsets for the analysis. NK and FL contributed to the interpretation of the results. HE provided the TROPOMI NO<sub>2</sub> data product and related information. All authors read and agreed on the published version of the paper.

### **Competing interests**

The authors declare that they have no conflict of interest.

**Acknowledgments.** Sentinel 5 Precursor TROPOMI Level 2 product is developed with funding from the Netherlands Space Office (NSO) and processed with funding from the European Space Agency (ESA). We also thank two anonymous reviewers for their detailed comments that helped us to improve the manuscript.

## Appendix

This appendix contains additional details of the used fitting algorithm that is largely based on the algorithm for multiple point source emission estimates (Fioletov et al., 2017). TROPOMI NO<sub>2</sub> VCD can be expressed as a sum of contributions  $\alpha_i \cdot \Omega_i$  from all individual industrial sources ( $i$ ), a population density-related term  $\alpha_p \Omega_p$ , an elevation-related background, and noise ( $\varepsilon$ ):

$$5 \quad TROPOMI \text{ NO}_2(\theta, \varphi) = \alpha_0 + \alpha_p \Omega_p(\theta, \varphi) + \sum \alpha_i \Omega_i(\theta, \varphi) + (\beta_0 + \beta_1(\theta - \theta_0) + \beta_2(\varphi - \varphi_0)) \cdot \exp(-H(\theta, \varphi)/H_0) + \varepsilon(\theta, \varphi) \quad (A1)$$

All  $\Omega$  function are normalized (i.e., their total integral equals to 1) plume functions: the value of that function for a particular pixel with latitude  $\theta$  and longitude  $\varphi$ , is proportional to the value of the plume parameterization from the source  $i$  located at the latitude  $\theta_i$  and longitude ( $\varphi_i$ ) (all in radian). The parameterization assumes that the plume is moving downwind along a straight line has a Gaussian shape spread across that line. To describe the plume, we can rotate satellite pixels for a particular  
 10 day around the source, so the plume would always be moving from north to south, apply the plume parameterization, and then rotate the pixels back. If  $(x_i, y_i)$  and  $(x'_i, y'_i)$  are the pixel's Cartesian coordinates (km) in the system with the origin at the source  $i$  before and after the rotation respectively, then they can be calculated from the pixel and source latitudes and longitudes as:

$$\begin{aligned} 15 \quad x_i &= r \cdot (\varphi - \varphi_i) \cdot \cos(\theta_i); \\ y_i &= r \cdot (\theta - \theta_i); \\ x'_i &= x_i \cdot \cos(-\omega) + y_i \cdot \sin(-\omega); \\ y'_i &= -x_i \cdot \sin(-\omega) + y_i \cdot \cos(-\omega); \end{aligned}$$

where  $r = 111.3 \text{ km} \cdot 180 / \pi$  (or  $r = 6371 \text{ km} \cdot \pi / 180$  for latitude and longitude in degrees);  $\omega$  is the pixel wind direction (0 for  
 20 north);  $\varphi_i$  and  $\theta_i$  are the source  $i$  longitude and latitude (all in radian). Note that there was a typo in this original formula for  $r$  in Fioletov et al., (2017).

Following Fioletov et al., (2017), the contribution  $\alpha_i \cdot \Omega_i = \alpha_i \Omega(\theta, \phi, \omega, s, \theta_i, \phi_i)$  from the source  $i$  can be expressed as  $\alpha_i \cdot \Omega_i = \alpha_i \cdot f(x'_i, y'_i) \cdot g(y'_i, s)$ , where:

$$\begin{aligned} 25 \quad f(x'_i, y'_i) &= \frac{1}{\sigma_1 \sqrt{2\pi}} \exp\left(-\frac{x'^2_i}{2\sigma_1^2}\right); \\ g(y'_i, s) &= \frac{\lambda_1}{2} \exp\left(\frac{\lambda_1(\lambda_1 \sigma^2 + 2y'_i)}{2}\right) \cdot \text{erfc}\left(\frac{\lambda_1 \sigma^2 + y'_i}{\sqrt{2}\sigma}\right); \\ \sigma_1 &= \begin{cases} \sqrt{\sigma^2 - 1.5y'_i}, & y'_i < 0; \\ \sigma, & y'_i \geq 0; \end{cases} \\ \lambda_1 &= \lambda/s; \end{aligned} \quad (A2)$$

It is assumed that NO<sub>2</sub> emitted from a point source decline exponentially (i.e., as  $\exp(-\lambda t)$ ) with time ( $t$ ) with a constant “lifetime” (or decay rate)  $\tau = 1/\lambda$ . The second parameter is the plume width ( $\sigma$ ).

Note that  $\int_{-\infty}^{\infty} \int_{-\infty}^{\infty} f(x, y) \cdot g(y, s) dx dy = \int_{-\infty}^{\infty} (\int_{-\infty}^{\infty} f(x, y) dx) \cdot g(y, s) dy = \int_{-\infty}^{\infty} g(y, s) dy = 1$ , therefore the parameter  $\alpha_i$  represents the total observed number of NO<sub>2</sub> molecules (or the NO<sub>2</sub> mass) near the source  $i$ . If *TROPOMI NO<sub>2</sub>* is in DU, and  $\sigma$  is in km, then  $a$  is in  $2.69 \cdot 10^{26}$  molec. or 0.021 T(NO<sub>2</sub>). Furthermore, the emission strength ( $E$ ) can be calculated as  $E = a/\tau$  assuming a simple mass balance.

5 As mentioned in section 3, some of the sources used in the analysis are not point sources but clusters. In that case,  $\Omega_i = \sum_j w_j \Omega_j(\theta, \phi, \omega, s, \theta_j, \phi_j)$ , where  $\Omega_j$  is the plume function for source  $j$  and  $w_j$  is the weighting coefficient established by the factor analysis.

Similarly,  $\alpha_p \Omega_p$  represent the contribution from the population density-related component, where  $\Omega_p$  is the plume function from an area-distributed source.  $\Omega_p$  is a weighted sum of plume functions from a grid with the weighting coefficients proportional to the population of at the grid points  $\Omega_p = \sum_{ij} \rho_{ij} \Omega(\theta, \phi, \omega, s, \theta_{ij}, \phi_{ij})$ , where  $\theta_{ij}, \phi_{ij}$  are the grid points coordinates and  $\rho_{ij}$  is the population associated with that grid points. Thus,  $\alpha_p$  is the coefficient that represent the total NO<sub>2</sub> mass the corresponds to one person. In our calculations we used 3° by 4° area with a 0.2° by 0.2° grid with 336 (16 x 21) grid cell.

15 Finally, the elevation-related background term  $\alpha_0 + (\beta_0 + \beta_1(\theta - \theta_0) + \beta_2(\varphi - \varphi_0)) \cdot \exp(-H/H_0)$ , where  $\theta_0$  and  $\varphi_0$  are the coordinates of the centre of the analyzed area and  $E$  is the elevation in km and  $H_0=1$  km, is determined by three parameters.

Equation (A1) represents a linear regression model where the unknown parameters  $\alpha_p, \alpha_i$  can be estimated from the measured variable (*TROPOMI NO<sub>2</sub>*) at many pixels and known regressors. The fitting was done three times using all data for the analysed period (March 16 – June 15) in 2018, 2019, and 2020.

## References

- Ass, KE, Eddaif, A, Radey, O, Aitzaouit, O, Yakoubi, ME, Chelhaoui, Y.: Effect of restricted emissions during Covid-19 lockdown on air quality in Rabat—Morocco. *Global NEST Journal* 22. DOI: <http://dx.doi.org/10.30955/gnj.003431>, 2020.
- Aydın, S, Nakiyingi, BA, Esmen, C, Gu'neysu, S, Ejjada, M.: Environmental impact of coronavirus (COVID-19) from Turkish perceptive. *Environment, Development and Sustainability*. DOI: <http://dx.doi.org/10.1007/s10668-020-00933-5>, 2020.
- Bao, R. and Zhang, A.: Does lockdown reduce air pollution? Evidence from 44 cities in northern China, *Sci. Total Environ.*, 731, doi:10.1016/j.scitotenv.2020.139052, 2020.
- Bar, S., Parida, B.R., Mandal, S.P., Pandey, A.C., Kumar, N., Mishra, B.: Impacts of partial to complete COVID-19 lockdown on NO<sub>2</sub> and PM<sub>2.5</sub> levels in major urban cities of Europe and USA, *Cities*, Volume 117, 103308, ISSN 0264-2751, <https://doi.org/10.1016/j.cities.2021.103308>, 2021.
- Barré, J., Petetin, H., Colette, A., Guevara, M., Peuch, V.-H., Rouil, L., Engelen, R., Inness, A., Flemming, J., Pérez García-Pando, C., Bowdalo, D., Meleux, F., Geels, C., Christensen, J. H., Gauss, M., Benedictow, A., Tsyro, S., Friese, E., Struzewska, J., Kaminski, J. W., Douros, J., Timmermans, R., Robertson, L., Adani, M., Jorba, O., Joly, M., and Kouznetsov, R.: Estimating lockdown-induced European NO<sub>2</sub> changes using satellite and surface observations and air quality models, *Atmos. Chem. Phys.*, 21, 7373–7394, <https://doi.org/10.5194/acp-21-7373-2021>, 2021.
- Bauwens, M., Compennolle, S., Stavrakou, T., Müller, J. F., van Gent, J., Eskes, H., Levelt, P. F., van der A, R., Veefkind, J. P., Vlietinck, J., Yu, H. and Zehner, C.: Impact of Coronavirus Outbreak on NO<sub>2</sub> Pollution Assessed Using TROPOMI and OMI Observations, *Geophys. Res. Lett.*, 47(11), 1–9, doi:10.1029/2020GL087978, 2020.
- Beirle, S., Platt, U., von Glasow, R., Wenig, M. and Wagner, T.: Estimate of nitrogen oxide emissions from shipping by satellite remote sensing, *Geophys. Res. Lett.*, 31(18), L18102, doi:10.1029/2004GL020312, 2004.
- Beirle, S., Boersma, K. F., Platt, U., Lawrence, M. G. and Wagner, T.: Megacity emissions and lifetimes of nitrogen oxides probed from space, *Science*, 333, 1737–1739, doi:10.1126/science.1207824, 2011.
- Beirle, S., Hörmann, C., Penning de Vries, M., Dörner, S., Kern, C. and Wagner, T.: Estimating the volcanic emission rate and atmospheric lifetime of SO<sub>2</sub> from space: a case study for Kīlauea volcano, Hawai'i, *Atmos. Chem. Phys.*, 14(16), 8309–8322, doi:10.5194/acp-14-8309-2014, 2014.
- Beirle, S., Borger, C., Dörner, S., Li, A., Hu, Z., Liu, F., Wang, Y. and Wagner, T.: Pinpointing nitrogen oxide emissions from space, *Sci. Adv.*, 5(11), doi:10.1126/sciadv.aax9800, 2019.
- Beirle, S., Borger, C., Dörner, S., Eskes, H., Kumar, V., de Laat, A., and Wagner, T.: Catalog of NO<sub>x</sub> emissions from point sources as derived from the divergence of the NO<sub>2</sub> flux for TROPOMI, *Earth Syst. Sci. Data*, 13, 2995–3012, <https://doi.org/10.5194/essd-13-2995-2021>, 2021.

- Belhekar, V. M.: Factor Analysis and Structural Equation Modeling, in A Step-by-Step Approach to Using SAS® for Factor Analysis and Structural Equation Modeling, Second Edition, edited by N. O'Rourke and L. Hatcher, pp. 314–361, SAS Institute., 2013.
- Bray, C. D., Nahas, A., Battye, W. H. and Aneja, V. P.: Impact of lockdown during the COVID-19 outbreak on multi-scale air quality, *Atmos. Environ.*, 254, 118386, doi:10.1016/j.atmosenv.2021.118386, 2021.
- Bucsela, E. J., Pickering, K. E., Allen, D. J., Holzworth, R. H. and Krotkov, N. A.: Midlatitude Lightning NO<sub>x</sub> Production Efficiency Inferred From OMI and WWLLN Data, *J. Geophys. Res. Atmos.*, 124, 13475–13497, doi:10.1029/2019JD030561, 2019.
- C3S: Copernicus Climate Change Service (C3S) : ERA5: Fifth generation of ECMWF atmospheric reanalyses of the global climate. Copernicus Climate Change Service Climate Data Store (CDS), [online] Available from: <https://cds.climate.copernicus.eu/cdsapp#!/home> (Accessed 20 June 2020), 2017.
- Chong, H., Lee, H., Koo, J.H., Kim, J., Jeong, U., Kim, W., Kim, S.W., Herman, J.R., Abuhassan, N.K., Ahn, J.Y., Park, J.H., Kim, S.K., Moon, K.J., Choi, W.J. and Park, S.S.: Regional Characteristics of NO<sub>2</sub> Column Densities from Pandora Observations during the MAPS-Seoul Campaign. *Aerosol Air Qual. Res.* 18: 2207–2219. <https://doi.org/10.4209/aaqr.2017.09.0341>, 2018.
- Collivignarelli, M. C., Abbà, A., Bertanza, G., Pedraz- zani, R., Ricciardi, P., and Carnevale Miino, M.: Lockdown for CoViD-2019 in Milan: What are the effects on air quality?, *Sci Total Environ*, 732, 139280–139280, <https://doi.org/10.1016/j.scitotenv.2020.139280>, 2020.
- Cunnold, D. M., Zawodny, J. M., Chu, W. P., Pommereau, J. P., Goutail, F., Lenoble, J., McCormick, M. P., Veiga, R. E., Murcray, D., Iwagami, N., Shibasaki, K., Simon, P. C. and Peetermans, W.: Validation of SAGE II NO<sub>2</sub> measurements, *J. Geophys. Res.*, 96, 12913, doi:10.1029/91JD01344, 1991.
- Dammers, E., McLinden, C. A. , Griffin, D., Shephard, M. W., van Der Graaf, S., Lutsch, E., Schaap, M., Gainairu-Matz, Y., Fioletov, V., van Damme, M., Whitburn, S., Clarisse, L., Cady-Pereira, K., Clerbaux, C., Francois Coheur, P. and Erisman, J.-W. J. W.: NH<sub>3</sub> emissions from large point sources derived from CrIS and IASI satellite observations, *Atmos. Chem. Phys.*, 19, 12261–12293, doi:10.5194/acp-19-12261-2019, 2019.
- Dantas, G, Siciliano, B, França, BB, da Silva, CM, Ar- billa, G. The impact of COVID-19 partial lock- down on the air quality of the city of Rio de Janeiro, Brazil. *Science of the Total Environment*, 729, DOI: <http://dx.doi.org/10.1016/j.scitotenv.2020.139085>. 2020.
- Dee, D. P., Uppala, S. M., Simmons, A. J., Berrisford, Poli, P., Kobayashi, S., Andrae, U., Balmaseda, M. A., Balsamo, G., Bauer, P., Bechtold, P., Beljaars, A. C. M., Berg, L. van de, Bidlot, J., Bormann, N., Delsol, C., Dragani, R., Fuentes, M., Geer, A. J., Haimberger, L., Healy, S. B., Hersbach, H., Hólm, E. V., Isaksen, I., Kållberg, P., Köhler, M., Matricardi, M., McNally, A. P., Monge-Sanz, B. M., Morcrette, J.-J., Park, B.-K., Peubey, C., Rosnay, P. de, Tavolato, C., Thépaut, J.-N. and Vitart, F.: The ERA-Interim reanalysis: Configuration and performance of the data assimilation system, *Q. J. R. Meteorol. Soc.*, 137, 553–597, doi:DOI: 10.1002/qj.828, 2011.



- Ding, J., van der A, R. J., Eskes, H. J., Mijling, B., Stavrakou, T., van Geffen, J. H. G. M. and Veefkind, J. P.: NO<sub>x</sub> Emissions Reduction and Rebound in China Due to the COVID-19 Crisis, *Geophys. Res. Lett.*, 47, e2020GL089912, doi:10.1029/2020GL089912, 2020.
- Duncan, B. N., Lamsal, L. N., Thompson, A. M., Yoshida, Y., Lu, Z., Streets, D. G., Hurwitz, M. M. and Pickering, K. E.: A space-based, high-resolution view of notable changes in urban NO<sub>x</sub> pollution around the world (2005–2014), *J. Geophys. Res. Atmos.*, 121, 976–996, doi:10.1002/2015JD024121, 2015.
- EC: European Commission: COVID-19 in European coal regions. [online] Available from: [https://ec.europa.eu/energy/sites/ener/files/documents/covid-19\\_in\\_european\\_coal\\_regions.pdf](https://ec.europa.eu/energy/sites/ener/files/documents/covid-19_in_european_coal_regions.pdf) (Accessed 1 March 2021), 2020.
- EPA: U.S. Environmental Protection Agency (EPA) National Emissions Inventory, [online] Available from: <https://www.epa.gov/air-emissions-inventories> (Accessed 17 July 2020), 2020.
- ESA EOP-GMQ: Sentinel-5 Precursor Calibration and Validation Plan for the Operational Phase, available at: <https://sentinel.esa.int/documents/247904/2474724/Sentinel-5P-Calibration-and-Validation-Plan.pdf> (last access: 29 August 2021), 2017.
- Fioletov, V., McLinden, C. A., Kharol, S. K., Krotkov, N. A., Li, C., Joiner, J., Moran, M. D., Vet, R., Visschedijk, A. J. H. and Denier Van Der Gon, H. A. C.: Multi-source SO<sub>2</sub> emission retrievals and consistency of satellite and surface measurements with reported emissions, *Atmos. Chem. Phys.*, 17, doi:10.5194/acp-17-12597-2017, 2017.
- Fioletov, V. E., McLinden, C. A., Krotkov, N. and Li, C.: Lifetimes and emissions of SO<sub>2</sub> from point sources estimated from OMI, *Geophys. Res. Lett.*, 42, doi:10.1002/2015GL063148, 2015.
- Fioletov, V. E., McLinden, C. A., Krotkov, N. A., Li, C., Joiner, J., Theys, N., Carn, S. and Moran, M. D.: A global catalogue of large SO<sub>2</sub> sources and emissions derived from the Ozone Monitoring Instrument, *Atmos. Chem. Phys.*, 16, 11497–11519, doi:10.5194/acp-16-11497-2016, 2016.
- de Foy, B., Wilkins, J. L., Lu, Z., Streets, D. G. and Duncan, B. N.: Model evaluation of methods for estimating surface emissions and chemical lifetimes from satellite data, *Atmos. Environ.*, 98, 66–77, doi:10.1016/j.atmosenv.2014.08.051, 2014.
- de Foy, B., Lu, Z., Streets, D. G., Lamsal, L. N. and Duncan, B. N.: Estimates of power plant NO<sub>x</sub> emissions and lifetimes from OMI NO<sub>2</sub> satellite retrievals, *Atmos. Environ.*, 116, 1–11, doi:10.1016/j.atmosenv.2015.05.056, 2015.
- van Geffen, J. H. G. M., Eskes, H. J., Boersma, K. F., Maasakkers, J. D. and Veefkind, J. P.: TROPOMI ATBD of the total and tropospheric NO<sub>2</sub> data products., [online] Available from: [http://www.tropomi.eu/sites/default/files/files/publicS5P-KNMI-L2-0005-RP-ATBD\\_NO2\\_data\\_products-20190206\\_v140.pdf](http://www.tropomi.eu/sites/default/files/files/publicS5P-KNMI-L2-0005-RP-ATBD_NO2_data_products-20190206_v140.pdf) (Accessed 17 June 2020), 2019.
- van Geffen, J., Eskes, H., Boersma, K., Maasakkers, J. and Veefkind, J.: TROPOMI ATBD of the total and tropospheric NO<sub>2</sub> data products (issue 1.2. 0), De Bilt, the Netherlands, s5P-KNMI-L2-0005-RP., 2018.
- van Geffen, J., Folkert Boersma, K., Eskes, H., Sneep, M., Ter Linden, M., Zara, M. and Pepijn Veefkind, J.: S5P TROPOMI

- NO<sub>2</sub> slant column retrieval: Method, stability, uncertainties and comparisons with OMI, *Atmos. Meas. Tech.*, 13(3), 1315–1335, doi:10.5194/amt-13-1315-2020, 2020.
- van Geffen, J., Eskes, H., Compernelle, S., Pinardi, G., Verhoelst, T., Lambert, J.-C., Sneep, M., ter Linden, M., Ludewig, A., Boersma, K. F., and Veefkind, J. P.: Sentinel-5P TROPOMI NO<sub>2</sub> retrieval: impact of version v2.2 improvements and comparisons with OMI and ground-based data, *Atmos. Meas. Tech. Discuss.* [preprint], <https://doi.org/10.5194/amt-2021-329>, in review, 2021. Gkatzelis, G. I., Gilman, J. B., Brown, S. S., Eskes, H., Gomes, A. R., Lange, A. C., McDonald, B. C., Peischl, J., Petzold, A., Thompson, C. R., and Kiendler-Scharr, A.: The Global Impacts of COVID-19 Lockdowns on Urban Air Quality: A Critical Review and Recommendations, *Elem. Sci. Anth.*, 9, doi:10.1525/elementa.2021.00176, 2021.
- 10 Fu, F, Purvis-Roberts, KL, Williams, B. Impact of the COVID-19 pandemic lockdown on air pollution in 20 major cities around the world. *Atmosphere* 11. DOI: <http://dx.doi.org/10.3390/atmos1111189>, 2020.
- Georgoulias, A. K., Boersma, K. F., Vliet, J. van, Zhang, X., A1, R. van der, Zanis, P. and Laat, J. de: Detection of NO<sub>2</sub> pollution plumes from individual ships with the TROPOMI/S5P satellite sensor, *Environ. Res. Lett.*, 10, 0–6, 2020.
- Ghahremanloo, M., Lops, Y., Choi, Y. and Mousavinezhad, S.: Impact of the COVID-19 outbreak on air pollution levels in East Asia, *Sci. Total Environ.*, 754, doi:10.1016/j.scitotenv.2020.142226, 2021.
- 15 Gkatzelis, G. I., Gilman, J. B., Brown, S. S., Eskes, H., Gomes, A. R., Lange, A. C., McDonald, B. C., Peischl, J., Petzold, A., Thompson, C. R. and Kiendler-Scharr, A.: The global impacts of COVID-19 lockdowns on urban air pollution: A critical review and recommendations, *Elementa*, 9, doi:10.1525/elementa.2021.00176, 2021.
- Goldberg, D. L., Anenberg, S. C., Griffin, D., McLinden, C. A., Lu, Z. and Streets, D. G.: Disentangling the impact of the COVID-19 lockdowns on urban NO<sub>2</sub> from natural variability, *Geophys. Res. Lett.*, doi:10.1029/2020GL089269, 2020.
- 20 Griffin, D., McLinden, C. A., Racine, J., Moran, M. D., Fioletov, V., Pavlovic, R., Mashayekhi, R., Zhao, X. and Eskes, H.: Assessing the impact of corona-virus-19 on nitrogen dioxide levels over southern Ontario, Canada, *Remote Sens.*, 12(24), 1–13, doi:10.3390/rs12244112, 2020.
- 25 Guevara, M., Jorba, O., Soret, A., Petetin, H., Bowdalo, D., Serradell, K., Tena, C., Van Der Gon, H. D., Kuenen, J., Peuch, V. H. and Pérez García-Pando, C.: Time-resolved emission reductions for atmospheric chemistry modelling in Europe during the COVID-19 lockdowns, *Atmos. Chem. Phys.*, 21, 773–797, doi:10.5194/acp-21-773-2021, 2021.
- Herman, J., Cede, A., Spinei, E., Mount, G., Tzortziou, M., and Abuhassan, N.: NO<sub>2</sub> column amounts from ground-based Pandora and MFDOAS spectrometers using the direct-sun DOAS technique: Intercomparisons and application to OMI validation, *J. Geophys. Res.*, 114, D13307, doi:10.1029/2009JD011848, 2009.
- 30 Hudman, R. C., Moore, N. E., Mebust, A. K., Martin, R. V., Russell, A. R., Valin, L. C. and Cohen, R. C.: Steps towards a mechanistic model of global soil nitric oxide emissions: Implementation and space based-constraints, *Atmos. Chem. Phys.*, 12, 7779–7795, doi:10.5194/acp-12-7779-2012, 2012.
- Judd, L. M., Al-Saadi, J. A., Szykman, J. J., Valin, L. C., Janz, S. J., Kowalewski, M. G., et al.: valuating Sentinel-5P

- TROPOMI tropospheric NO<sub>2</sub> column densities with airborne and Pandora spectrometers near New York City and Long Island Sound. *Atmospheric Measurement Techniques*, 13, 6113–6140. <https://doi.org/10.5194/amt-13-6113-2020>, 2020.
- 5 Ialongo, I., Virta, H., Eskes, H., Hovila, J., and Douros, J.: Comparison of TROPOMI/Sentinel-5 Precursor NO<sub>2</sub> observations with ground-based measurements in Helsinki, *Atmos. Meas. Tech.*, 13, 205–218, <https://doi.org/10.5194/amt-13-205-2020>, 2020.
- Juncosa Calahorrano, J. F., Lindaas, J., O'Dell, K., Palm, B. B., Peng, Q., Flocke, F., Pollack, I. B., Garofalo, L. A., Farmer, D. K., Pierce, J. R., Collett, J. L., Weinheimer, A., Campos, T., Hornbrook, R. S., Hall, S. R., Ullmann, K., Pothier, M. A., Apel, E. C., Permar, W., Hu, L., Hills, A. J., Montzka, D., Tyndall, G., Thornton, J. A. and Fischer, E. V.: Daytime Oxidized Reactive Nitrogen Partitioning in Western U.S. Wildfire Smoke Plumes, *J. Geophys. Res. Atmos.*, 126, e2020JD033484, doi:10.1029/2020JD033484, 2021.
- 10 Kenagy, H. S., Sparks, T. L., Ebben, C. J., Wooldrige, P. J., Lopez-Hilfiker, F. D., Lee, B. H., et al.: NO<sub>x</sub> lifetime and NO<sub>y</sub> partitioning during WINTER. *Journal of Geophysical Research: Atmospheres*, 123, 9813–9827. <https://doi.org/10.1029/2018JD028736>, 2018
- 15 Kanniah, K. D., Kamarul Zaman, N. A. F., Kaskaoutis, D. G. and Latif, M. T.: COVID-19's impact on the atmospheric environment in the Southeast Asia region, *Sci. Total Environ.*, 736, 139658, doi:10.1016/j.scitotenv.2020.139658, 2020.
- Keller, C. A., Evans, M. J., Emma Knowland, K., Hasenkopf, C. A., Modekurty, S., Lucchesi, R. A., Oda, T., Franca, B. B., Mandarino, F. C., Valeria Díaz Suárez, M., Ryan, R. G., Fakes, L. H. and Pawson, S.: Global impact of COVID-19 restrictions on the surface concentrations of nitrogen dioxide and ozone, *Atmos. Chem. Phys.*, 21, 3555–3592, doi:10.5194/acp-21-3555-2021, 2021.
- 20 Kim, Minsu, Gerrit, Kuhlmann, Dominik, Brunner, Dataset for: Importance of satellite observations for high-resolution mapping of near-surface NO<sub>2</sub> by machine learning. *Remote Sensing of Environment*, 264, 112573, <https://doi.org/10.1016/j.rse.2021.112573>, 2021.
- 25 Kondragunta, S., Wei, Z., McDonald, B. C., Goldberg, D. L., & Tong, D. Q. COVID-19 induced fingerprints of a new normal urban air quality in the United States. *Journal of Geophysical Research: Atmospheres*, 126, e2021JD034797. <https://doi.org/10.1029/2021JD034797>, 2021.
- Konovalov, I. B., Beekmann, M., Richter, A. and Burrows, J. P.: Inverse modelling of the spatial distribution of NO<sub>x</sub> emissions on a continental scale using satellite data, *Atmos. Chem. Phys.*, 6, 1747–1770, doi:10.5194/acp-6-1747-2006, 2006.
- 30 Koukouli, M. E., Skoulidou, I., Karavias, A., Parcharidis, I., Balis, D., Manders, A., Segers, A., Eskes, H. and Van Geffen, J.: Sudden changes in nitrogen dioxide emissions over Greece due to lockdown after the outbreak of COVID-19, *Atmos. Chem. Phys.*, 21, 1759–1774, doi:10.5194/acp-21-1759-2021, 2021.
- Krotkov, N. A., McLinden, C. A., Li, C., Lamsal, L. N., Celarier, E. A., Marchenko, S. V., Swartz, W. H., Bucsela, E. J., Joiner, J., Duncan, B. N., Boersma, K. F., Veefkind, J. P., Levelt, P. F., Fioletov, V. E., Dickerson, R. R., He, H., Lu,

- Z. and Streets, D. G.: Aura OMI observations of regional SO<sub>2</sub> and NO<sub>2</sub> pollution changes from 2005 to 2015, *Atmos. Chem. Phys.*, 16, 4605–4629, doi:10.5194/acp-16-4605-2016, 2016.
- Lamsal, L. N., Martin, R. V., Parrish, D. D. and Krotkov, N. A.: Scaling relationship for NO<sub>2</sub> pollution and urban population size: A satellite perspective, *Environ. Sci. Technol.*, 47, 7855–7861, doi:10.1021/es400744g, 2013.
- 5 Lamsal, L. N., Duncan, B. N., Yoshida, Y., Krotkov, N. a., Pickering, K. E., Streets, D. G. and Lu, Z.: U.S. NO<sub>2</sub> trends (2005–2013): EPA Air Quality System (AQS) data versus improved observations from the Ozone Monitoring Instrument (OMI), *Atmos. Environ.*, 110, 130–143, doi:10.1016/j.atmosenv.2015.03.055, 2015.
- Lamsal, L. N., Krotkov, N. A., Vasilkov, A., Marchenko, S., Qin, W., Yang, E.-S., Fasnacht, Z., Joiner, J., Choi, S., Haffner, D., Swartz, W. H., Fisher, B., and Bucsel, E.: Ozone Monitoring Instrument (OMI) Aura nitrogen dioxide standard product version 4.0 with improved surface and cloud treatments, *Atmos. Meas. Tech.*, 14, 455–479, <https://doi.org/10.5194/amt-14-455-2021>, 2021.
- 10 Lange, K., Richter, A. and Burrows, J. P.: Variability of nitrogen oxide lifetimes and emission fluxes estimated by Sentinel-5P observations, *Atmos. Chem. Phys. Discuss.*, doi:<https://doi.org/10.5194/acp-2021-273>, 2021.
- Laughner, J. and Cohen, R. C.: Direct observation of changing NO<sub>x</sub> lifetime in North American cities, *Science*, 366 (6466), 723–727 [online] Available from: <https://science.sciencemag.org/content/366/6466/723.full>, 2019.
- 15 Lee, J. D., Drysdale, W. S., Finch, D. P., Wilde, S. E., and Palmer, P. I.: UK surface NO<sub>2</sub> levels dropped by 42 % during the COVID-19 lockdown: impact on surface O<sub>3</sub>, *Atmos. Chem. Phys.*, 20, 15743–15759, <https://doi.org/10.5194/acp-20-15743-2020>, 2020.
- Levelt, P. F., Joiner, J., Tamminen, J., Veefkind, J. P., Bhartia, P. K., Fioletov, V., Carn, S., Laatz, J. De, Deland, M., Marchenko, S. and McPeters, R.: The Ozone Monitoring Instrument : overview of 14 years in space, *Atmos. Chem. Phys.*, 18, 5699–5745, doi:<https://doi.org/10.5194/acp-18-5699-2018>, 2018.
- 20 Levelt, P. F., Stein Zweers, D. C., Aben, I., Bauwens, M., Borsdorff, T., De Smedt, I., Eskes, H. J., Lerot, C., Loyola, D. G., Romahn, F., Stavrou, T., Theys, N., Van Roozendaal, M., Veefkind, J. P., and Verhoelst, T.: Air quality impacts of COVID-19 lockdown measures detected from space using high spatial resolution observations of multiple trace gases from Sentinel-5P/TROPOMI, *Atmos. Chem. Phys. Discuss.*, <https://doi.org/10.5194/acp-2021-534>, in review, 2021.
- 25 Liu, F., Beirle, S., Zhang, Q., Dörner, S., He, K. and Wagner, T.: NO<sub>x</sub> lifetimes and emissions of cities and power plants in polluted background estimated by satellite observations, *Atmos. Chem. Phys.*, 16, 5283–5298, doi:10.5194/acp-16-5283-2016, 2016.
- 30 Liu, F., Choi, S., Li, C., Fioletov, V. E., McLinden, C. A. and Joiner, J.: A new global anthropogenic SO<sub>2</sub> emission inventory for the last decade : a mosaic of satellite-derived and bottom-up emissions, *Atmos. Chem. Phys.*, 18, 16571–16586, 2018.
- Liu, F., Page, A., Strode, S. A., Yoshida, Y., Choi, S., Zheng, B., Lamsal, L. N., Li, C., Krotkov, N. A., Eskes, H., Ronald Vander, A., Veefkind, P., Levelt, P., Joiner, J. and Hauser, O. P.: Abrupt declines in tropospheric nitrogen dioxide

over China after the outbreak of COVID-19, arXiv, (2), 2–7, 2020a.

- Liu, F., Page, A., Strode, S.A., Yoshida, Y., Choi, S., Smith, S., Knowland, K.E., Zheng, B., Lamsal, L.N., Li, C. and Krotkov, N.A., Abrupt decline in tropospheric nitrogen dioxide after the outbreak of COVID-19. In AGU Fall Meeting 2020. AGU, 2020b.
- 5 Lorente, A., Boersma, K. F., Eskes, H. J., Veefkind, J. P., van Geffen, J. H. G. M., de Zeeuw, M. B., Denier van der Gon, H. A. C., Beirle, S. and Krol, M. C.: Quantification of nitrogen oxides emissions from build-up of pollution over Paris with TROPOMI, *Sci. Rep.*, 9, 1–10, doi:10.1038/s41598-019-56428-5, 2019.
- Lu, Z., Streets, D. G., De Foy, B., Lamsal, L. N., Duncan, B. N. and Xing, J.: Emissions of nitrogen oxides from US urban areas: Estimation from Ozone Monitoring Instrument retrievals for 2005–2014, *Atmos. Chem. Phys.*, 15, 10367–
- 10 10383, doi:10.5194/acp-15-10367-2015, 2015.
- Martin, R. V., Chance, K., Jacob, D. J., Kurosu, T. P., Spurr, R. J. D., Bucsela, E., Gleason, J. F., Palmer, P. I., Bey, I., Fiore, A. M., Li, Q., Yantosca, R. M. and Koelemeijer, R. B. A.: An improved retrieval of tropospheric nitrogen dioxide from GOME, *J. Geophys. Res. D Atmos.*, 107, doi:10.1029/2001JD001027, 2002.
- McLinden, C. A., Fioletov, V., Boersma, K. F., Krotkov, N., Sioris, C. E., Veefkind, J. P. and Yang, K.: Air quality over the
- 15 Canadian oil sands: A first assessment using satellite observations, *Geophys. Res. Lett.*, 39, 1–8, doi:10.1029/2011GL050273, 2012.
- McLinden, C. A., Fioletov, V., Shephard, M. W., Krotkov, N., Li, C., Martin, R. V., Moran, M. D. and Joiner, J.: Space-based detection of missing sulfur dioxide sources of global air pollution, *Nat. Geosci.*, 9, 496–500, doi:10.1038/ngeo2724, 2016.
- 20 McLinden, C. A., Adams, C. L. F., Fioletov, V., Griffin, D., Makar, P. A., Zhao, X., Kovachik, A., Dickson, N. M., Brown, C., Krotkov, N., Li, C., Theys, N., Hedelt, P. and Loyola, D. G.: Inconsistencies in sulphur dioxide emissions from the Canadian oil sands and potential implications, *Environ. Res. Lett.*, 16, doi:10.1088/1748-9326/abcbbb, 2020.
- Mehmood K, Bao Y, Petropoulos GP, Abbas R, Abrar MM, Saifullah, Mustafa A, Soban A, Saud S, Ahmad M, Hussain I, Fahad S. Investigating connections between COVID-19 pandemic, air pollution and community interventions for
- 25 Pakistan employing geoinformation technologies, *Chemosphere*, 272:129809. doi: 10.1016/j.chemosphere.2021.129809. Epub 2021 Jan 29. PMID: 33582510; PMCID: PMC7846247, 2021
- Mijling, B. and Van Der A, R. J.: Using daily satellite observations to estimate emissions of short-lived air pollutants on a mesoscopic scale, *J. Geophys. Res. Atmos.*, 117(17), 17302, doi:10.1029/2012JD017817, 2012.
- Miller, S. D., Mills, S. P., Elvidge, C. D., Lindsey, D. T., Lee, T. F. and Hawkins, J. D.: Suomi satellite brings to light a unique
- 30 frontier of nighttime environmental sensing capabilities, *Proc. Natl. Acad. Sci. U. S. A.*, 109, 15706–15711, doi:10.1073/pnas.1207034109, 2012.
- Misra, P., Takigawa, M., Khatri, P., Dhaka, S.K., Dimri, A.P., Yamaji, K., Kajino, M., Takeuchi, W., Imasu, R., Nitta, K., Patra, P.K., Hayashida, S.; Nitrogen oxides concentration and emission change detection during COVID-19 restrictions in North India (2021) *Scientific Reports*, 11, art. no. 9800

- NOAA: 2-Minute Gridded Global Relief Data (ETOPO2v2), [online] Available from:  
<https://www.ngdc.noaa.gov/mgg/global/etopo2.html> (Accessed 17 June 2020), 2006.
- NPRI: National Pollutant Release Inventory (NPRI). Sulfur oxide emissions for Canada, [online] Available from:  
[www.canada.ca/en/services/environment/pollution-waste-management/national-pollutant-release-inventory.html](http://www.canada.ca/en/services/environment/pollution-waste-management/national-pollutant-release-inventory.html)  
5 (Accessed 17 July 2020), 2020.
- Pommier, M., McLinden, C. A. and Deeter, M.: Relative changes in CO emissions over megacities based on observations from space, *Geophys. Res. Lett.*, 40, 3766–3771, doi:10.1002/grl.50704, 2013.
- Potts, D.A., Marais, E.A., Boesch, H., Pope, R.J., Lee, J., Drysdale, W., Chipperfield, M.P., Kerridge, B., Siddans, R., Moore, D.P., Remedios, J. Diagnosing air quality changes in the UK during the COVID-19 lockdown using TROPOMI and  
10 GEOS-Chem (2021) *Environmental Research Letters*, 16, art. no. 054031, 2021.
- Qu, Z., Jacob, D. J., Silvern, R. F., Shah, V., Campbell, P. C., Valin, L. C. and Murray, L. T.: US COVID-19 shutdown demonstrates importance of background NO<sub>2</sub> in inferring NO<sub>x</sub> emissions from satellite NO<sub>2</sub> observations, *Geophys. Res. Lett.*, 48(10), doi:10.1029/2021GL092783, 2021.
- Richter, A., Eyring, V., Burrows, J. P., Bovensmann, H., Lauer, A., Sierk, B. and Crutzen, P. J.: Satellite measurements of  
15 NO<sub>2</sub> from international shipping emissions, *Geophys. Res. Lett.*, 31(23), 1–4, doi:10.1029/2004GL020822, 2004.
- Sannigrahi S., P. Kumar, A. Molter, Q. Zhang, B. Basu, A. S. Basu, F. Pilla, Examining the status of improved air quality in world cities due to COVID-19 led temporary reduction in anthropogenic emissions, *Environmental Research*, 196,, 110927, <https://doi.org/10.1016/j.envres.2021.110927>, 2021
- SEDAC: The Gridded Population of the World (GPW), [online] Available from:  
20 <https://sedac.ciesin.columbia.edu/data/collection/gpw-v4>, 2017.
- Sha, T., Ma, X., Zhang, H., Janecek, N., Wang, Y., Wang, Y., Castro Garcíá, L., Jenerette, G. D. and Wang, J.: Impacts of Soil NO<sub>x</sub>Emission on O<sub>3</sub>Air Quality in Rural California, *Environ. Sci. Technol.*, doi:10.1021/acs.est.0c06834, 2021.
- Siciliano, B.; Carvalho, G.; Da Silva, C.M.; Arbillá, G. The Impact of COVID-19 Partial Lockdown on Primary Pollutant Concentrations in the Atmosphere of Rio de Janeiro and São Paulo Megacities (Brazil). *Bull. Environ. Contam. Toxicol.*, 105, 2–8, 2020.  
25
- Silvern, R. F., Jacob, D. J., Mickley, L. J., Sulprizio, M. P., Travis, K. R., Marais, E. A., Cohen, R. C., Laughner, J. L., Choi, S., Joiner, J. and Lamsal, L. N.: Using satellite observations of tropospheric NO<sub>2</sub> columns to infer long-term trends in US NO<sub>x</sub> emissions: The importance of accounting for the free tropospheric NO<sub>2</sub> background, *Atmos. Chem. Phys.*, 19(13), 8863–8878, doi:10.5194/acp-19-8863-2019, 2019.
- 30 Stavrakou, T., Müller, J. F., Bauwens, M., Boersma, K. F. and van Geffen, J.: Satellite evidence for changes in the NO<sub>2</sub> weekly cycle over large cities, *Sci. Rep.*, 10, 1–9, doi:10.1038/s41598-020-66891-0, 2020.
- Streets, D. G., Canty, T., Carmichael, G. R., De Foy, B., Dickerson, R. R., Duncan, B. N., Edwards, D. P., Haynes, J. A., Henze, D. K., Houyoux, M. R., Jacob, D. J., Krotkov, N. A., Lamsal, L. N., Liu, Y., Lu, Z., Martin, R. V., Pfister, G. G., Pinder, R. W., Salawitch, R. J. and Wecht, K. J.: Emissions estimation from satellite retrievals: A review of current

capability, *Atmos. Environ.*, 77, 1011–1042, doi:10.1016/j.atmosenv.2013.05.051, 2013.

- Tack, F., Merlaud, A., Iordache, M.-D., Pinardi, G., Dimitropoulou, E., Eskes, H., Bomans, B., Veefkind, P., and Van Roozendael, M.: Assessment of the TROPOMI tropospheric NO<sub>2</sub> product based on airborne APEX observations, *Atmos. Meas. Tech.*, 14, 615–646, <https://doi.org/10.5194/amt-14-615-2021>, 2021.
- Vadrevu, K. P., Eaturu, A., Biswas, S., Lasko, K., Sahu, S., Garg, J. K. and Justice, C.: Spatial and temporal variations of air pollution over 41 cities of India during the COVID-19 lockdown period, *Sci. Rep.*, 10, 1–15, doi:10.1038/s41598-020-72271-5, 2020.
- Theys, N., Fioletov, V., Li, C., De Smedt, I., Lerot, C., McLinden, C., et al. (2021). A Sulfur Dioxide Covariance-Based Retrieval Algorithm (COBRA): application to TROPOMI reveals new emission sources. *Atmos. Chem. Phys.*, 1–42. doi:10.5194/acp-2021-294.
- Veefkind, J. P. P., Aben, I., McMullan, K., Förster, H., de Vries, J., Otter, G., Claas, J., Eskes, H. J. J., de Haan, J. F. F., Kleipool, Q., van Weele, M., Hasekamp, O., Hoogeveen, R., Landgraf, J., Snel, R., Tol, P., Ingmann, P., Voors, R., Kruizinga, B., Vink, R., Visser, H. and Levelt, P. F. F.: TROPOMI on the ESA Sentinel-5 Precursor: A GMES mission for global observations of the atmospheric composition for climate, air quality and ozone layer applications, *Remote Sens. Environ.*, 120, 70–83, doi:10.1016/j.rse.2011.09.027, 2012.
- Venter, Z. S., Aunan, K., Chowdhury, S. Jos Lelieveld, J.: COVID-19 lockdowns cause global air pollution declines, *PNAS* 117, 18984–18990;; <https://doi.org/10.1073/pnas.2006853117>, 2020.
- Verhoelst, T., Compernolle, S., Pinardi, G., Lambert, J. C., Eskes, H. J., Eichmann, K. U., Fjæraa, A. M., Granville, J., Niemeijer, S., Cede, A., Tiefengraber, M., Hendrick, F., Pazmiño, A., Bais, A., Bazureau, A., Folkert Boersma, K., Bogner, K., Dehn, A., Donner, S., Elokhov, A., Gebetsberger, M., Goutail, F., Grutter De La Mora, M., Gruzdev, A., Gratsea, M., Hansen, G. H., Irie, H., Jepsen, N., Kanaya, Y., Karagkiozidis, D., Kivi, R., Kreher, K., Levelt, P. F., Liu, C., Müller, M., Navarro Comas, M., PETERS, A. J. M., Pommereau, J. P., Portafaix, T., Prados-Roman, C., Puertedura, O., Querel, R., Remmers, J., Richter, A., Rimmer, J., Cárdenas, C. R., De Miguel, L. S., Sinyakov, V. P., Stremme, W., Strong, K., Van Roozendael, M., Pepijn Veefkind, J., Wagner, T., Wittrock, F., Yela González, M. and Zehner, C.: Ground-based validation of the Copernicus Sentinel-5P TROPOMI NO<sub>2</sub> measurements with the NDACC ZSL-DOAS, MAX-DOAS and Pandonia global networks, *Atmos. Meas. Tech.*, 14(1), 481–510, doi:10.5194/amt-14-481-2021, 2021.
- Vinnikov, K. Y., Dickerson, R. R., Krotkov, N. A., Edgerton, E. S. and Schwab, J. J.: The net decay time of anomalies in concentrations of atmospheric pollutants, *Atmos. Environ.*, 160, 19–26, doi:10.1016/j.atmosenv.2017.04.006, 2017.
- Virghileanu, M., Săvulescu, I., Mihai, B. A., Nistor, C. and Dobre, R.: Nitrogen dioxide (No<sub>2</sub>) pollution monitoring with sentinel-5p satellite imagery over europe during the coronavirus pandemic outbreak, *Remote Sens.*, 12, 1–29, doi:10.3390/rs12213575, 2020.
- Williams, J. E., Folkert Boersma, K., Le Sager, P. and Verstraeten, W. W.: The high-resolution version of TM5-MP for optimized satellite retrievals: Description and validation, *Geosci. Model Dev.*, 10(2), 721–750, doi:10.5194/gmd-10-721-2017, 2017.
- Zhao, X., Griffin, D., Fioletov, V., McLinden, C., Cede, A., Tiefengraber, M., Müller, M., Bogner, K., Strong, K., Boersma,

F., Eskes, H., Davies, J., Ogyu, A., and Lee, S. C.: Assessment of the quality of TROPOMI high-spatial-resolution NO<sub>2</sub> data products in the Greater Toronto Area, *Atmos. Meas. Tech.*, 13, 2131–2159, <https://doi.org/10.5194/amt-13-2131-2020>, 2020.

5 Zhang, H., Lin, Y., Wei, S., Loo, B. P. Y., Lai, P. C., Lam, Y. F., Wan, L. and Li, Y.: Global association between satellite-derived nitrogen dioxide (NO<sub>2</sub>) and lockdown policies under the COVID-19 pandemic, *Sci. Total Environ.*, 761, 144148, doi:10.1016/j.scitotenv.2020.144148, 2021.

10 Zhang, L., Jacob, D. J., Knipping, E. M., Kumar, N., Munger, J. W., Carouge, C. C., van Donkelaar, A., Wang, Y. X., and Chen, D.: Nitrogen deposition to the United States: distribution, sources, and processes, *Atmos. Chem. Phys.*, 12, 4539–4554, <https://doi.org/10.5194/acp-12-4539-2012>, 2012. Zoogman, P., Liu, X., Suleiman, R. M., Pennington, W. F., Flittner, D. E., Al-Saadi, J. A., Hilton, B. B., Nicks, D. K., Newchurch, M. J., Carr, J. L., Janz, S. J., Andraschko, M. R., Arola, A., Baker, B. D., Canova, B. P., Chan Miller, C., Cohen, R. C., Davis, J. E., Dussault, M. E., Edwards, D. P., Fishman, J., Ghulam, A., González Abad, G., Grutter, M., Herman, J. R., Houck, J., Jacob, D. J., Joiner, J., Kerridge, B. J., Kim, J., Krotkov, N. A., Lamsal, L., Li, C., Lindfors, A., Martin, R. V., McElroy, C. T., McLinden, C., Natraj, V., Neil, D. O., Nowlan, C. R., O’Sullivan, E. J., Palmer, P. I., Pierce, R. B., Pippin, M. R., Saiz-Lopez, A., Spurr, R. J. D., Szykman, J. J., Torres, O., Veefkind, J. P., Veiðhelmann, B., Wang, H., Wang, J. and Chance, K.: Tropospheric emissions: Monitoring of pollution (TEMPO), *J. Quant. Spectrosc. Radiat. Transf.*, doi:10.1016/j.jqsrt.2016.05.008, 2016.

15



**Table 1.** The standard deviations of the random errors and interannual variability for background, urban and industrial components for the U.S. and Canada in percent. The random errors are calculated as the averages of estimates for individual years. The interannual variability estimates are the standard deviations calculated from three years (2018, 2019, and 2021). Interannual variability of the industrial component is calculated for regions with estimated total emissions greater than 1 kt yr<sup>-1</sup>.

Area	Random Error (%)			Interannual Variability (%)		
	Background	Urban	Industrial	Background	Urban	Industrial
Atlanta	0.20	1.04	1.47	5.9	9.7	11.3
Boston	0.29	0.93	5.68	4.0	10.8	39.3
Calgary	0.27	1.62	2.40	7.5	3.5	23.8
Charlotte	0.25	1.80	2.64	5.1	7.0	19.2
Chicago	0.27	0.73	1.74	17.5	9.3	11.6
Dallas	0.20	0.82	2.34	5.8	9.2	6.2
Denver	0.27	0.89	2.29	4.0	7.8	17.5
Detroit	0.27	0.99	2.17	13.3	5.5	16.8
Edmonton	0.34	0.80	1.91	11.0	15.6	8.1
Houston	0.22	0.78	1.25	6.7	13.0	10.5
Las Vegas	0.12	0.48		7.6	16.7	
Los Angeles	0.22	0.22		1.4	9.2	
Miami	0.15	0.88	2.66	1.9	5.8	40.7
Minneapolis	0.20	1.42	3.28	15.1	10.1	29.5
Montreal	0.29	1.21	3.24	11.8	7.3	19.7
New York	0.36	0.41	5.17	8.2	5.8	8.0
Orlando	0.17	1.17	2.16	4.0	10.6	16.5
Phoenix	0.17	0.75	2.84	4.9	17.0	23.5
Pittsburgh	0.33	1.62	2.20	6.5	6.3	7.0
Portland	0.29	0.87	4.32	5.8	21.2	23.2
San Antonio	0.18	1.50	1.20	8.1	5.9	42.0
San Francisco	0.17	0.64	4.64	1.1	12.8	20.9
Seattle	0.31	1.14	2.71	9.0	11.0	18.9
St. Louis	0.20	1.48	1.87	16.3	4.5	7.8
Toronto	0.29	0.78	1.97	10.8	12.9	13.7
Vancouver	0.49	0.74	5.74	2.1	9.6	14.7
Washington	0.24	1.03	2.76	6.8	13.2	8.0
Average	0.25	0.99	2.82	7.5	10.0	18.3
Standard deviation	0.08	0.4	1.3	4.4	4.3	10

**Table 2.** The standard deviations of the random errors and interannual variability for background, urban and industrial components for 13 regions in percent. The random errors and interannual variability are calculated from three years (2018, 2019, and 2021) for each area and then averaged for all areas in the region. Interannual variability of the industrial component is calculated for regions with estimated total emissions greater than 1 kt yr<sup>-1</sup>.

Area	Random Error (%)			Interannual Variability (%)		
	Background	Urban	Industrial	Background	Urban	Industrial
Africa	0.21	1.56	2.42	7.3	19.8	21.3
Australia and New Zealand	0.34	0.80	1.22	8.6	9.2	12.2
Canada and US	0.25	0.99	2.82	7.5	10.0	18.3
Central America	0.21	0.95	1.72	5.4	11.0	20.3
China	0.30	1.06	1.90	7.3	19.6	16.4
Europe-1	0.23	0.96	4.06	5.6	12.3	27.6
Europe-2	0.25	1.30	3.13	6.8	15.4	17.1
India	0.23	1.78	0.77	9.0	16.6	12.4
Japan Korea, Taiwan	0.31	0.86	1.29	4.9	12.9	13.2
Middle East	0.29	1.43	0.86	7.5	22.2	19.9
Northern Eurasia	0.29	1.42	2.78	8.8	13.5	25.4
South America	0.39	2.97	6.72	7.8	18.6	23.6
South-East Asia	0.29	1.03	1.68	8.0	14.1	16.1
Average	0.28	1.32	2.41	7.3	15.0	18.8
Standard deviation	0.05	0.58	1.61	1.3	4.1	4.9

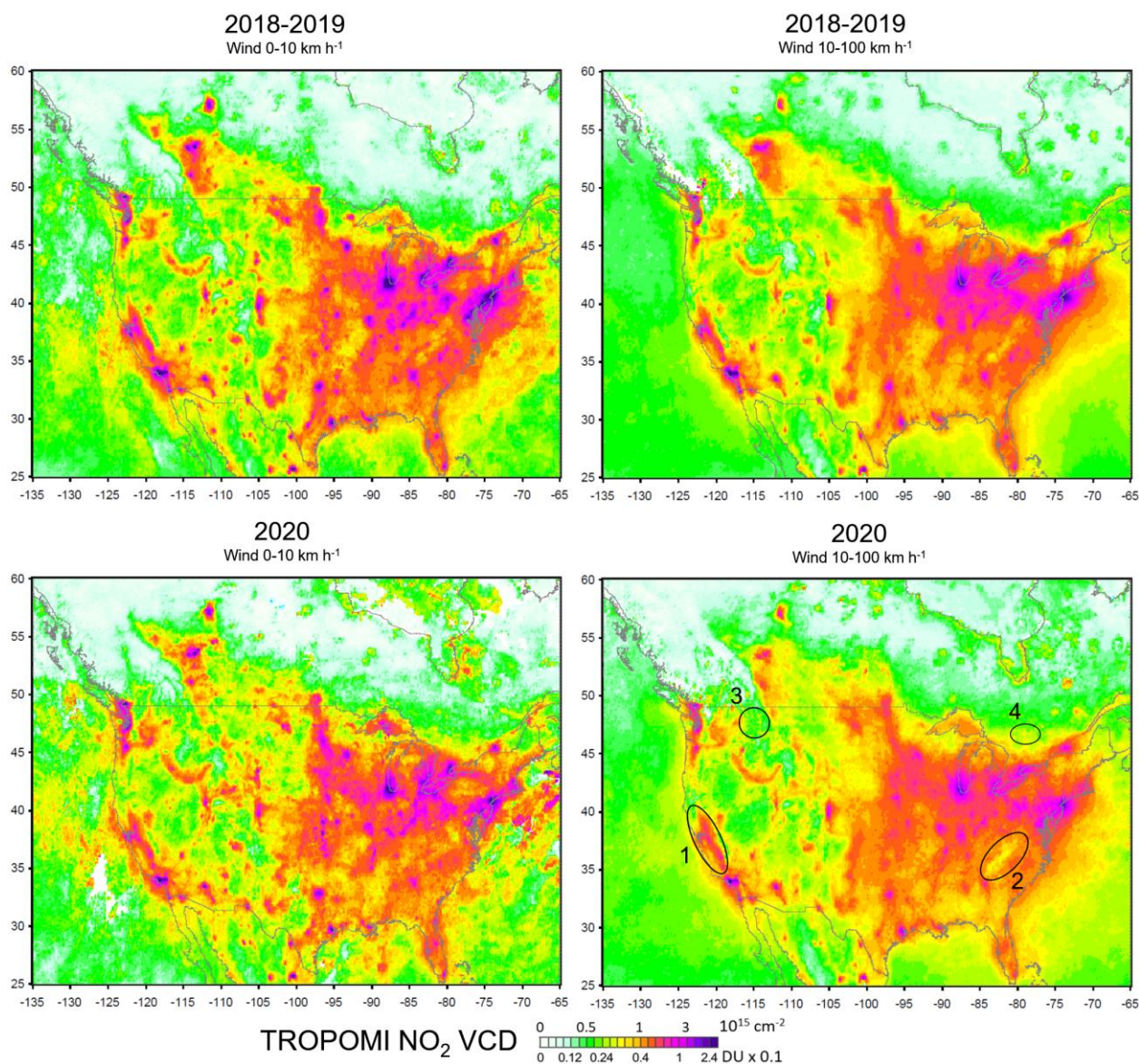


**Figure 1.** Mean TROPOMI NO<sub>2</sub> VCDs over the US and southern Canada for March 16–June 15, in (top) 2018-2019 and (bottom) 2020. The main features of the NO<sub>2</sub> distribution such as elevated NO<sub>2</sub> values over large cities, industrial sources and in the valleys such as the California Central Valley (1) and lower values over the mountains such as Appalachian (2) are evident from the plot. Note, that NO<sub>2</sub> VCDs are not negligible (about  $5 \cdot 10^{14}$  cm<sup>-2</sup>) even over vast remote areas such as National Forests in Montana (3) or Algonquin Provincial Park in Ontario (4) as well as over the oceans. The maps are based on Level 2 data gridded on 0.1° by 0.1° grid grouped by the wind speed: (left) less than 10 km per hour and (right) more than 10 km per hour.

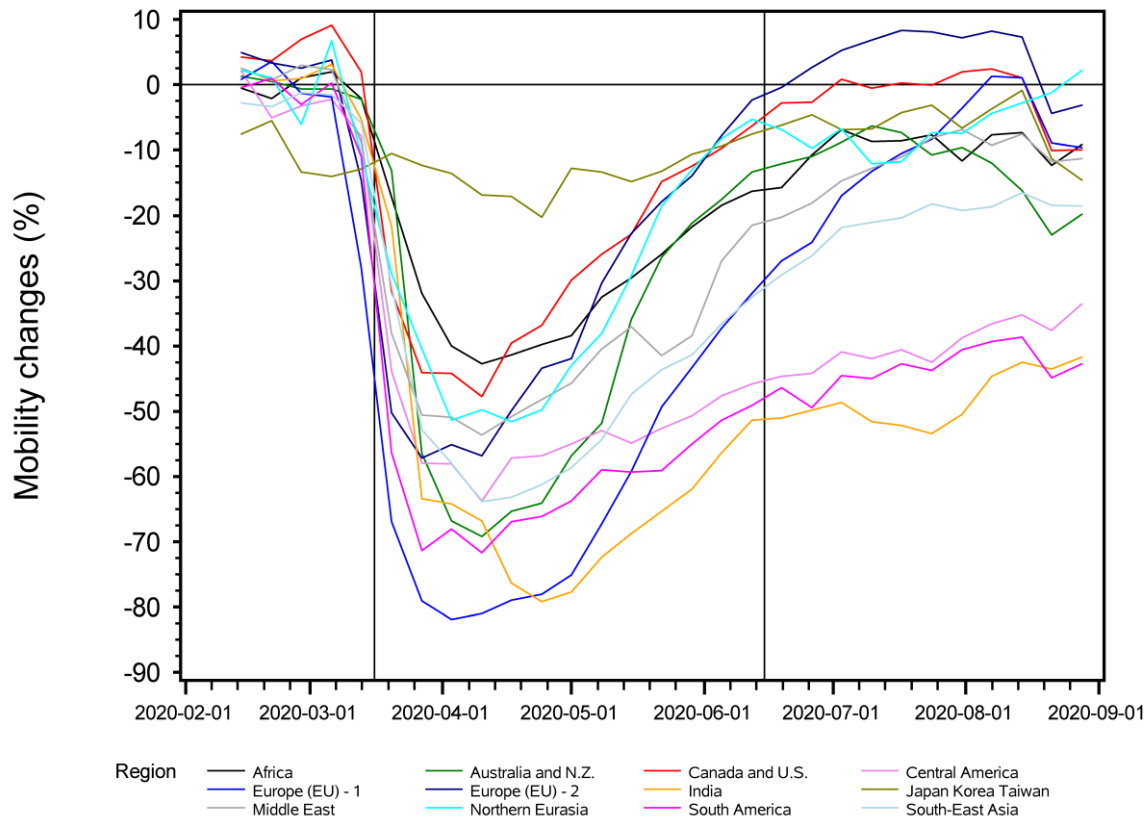


**Figure 2.** Changes in weekly Google mobility data (for “retail and recreation” category) relative to the baseline period (Jan 3 – Feb 6, 2020) for twelve regions analysed in this study. The black vertical lines represent the beginning and the end of the period analyzed in this study (March 16 – June 15).

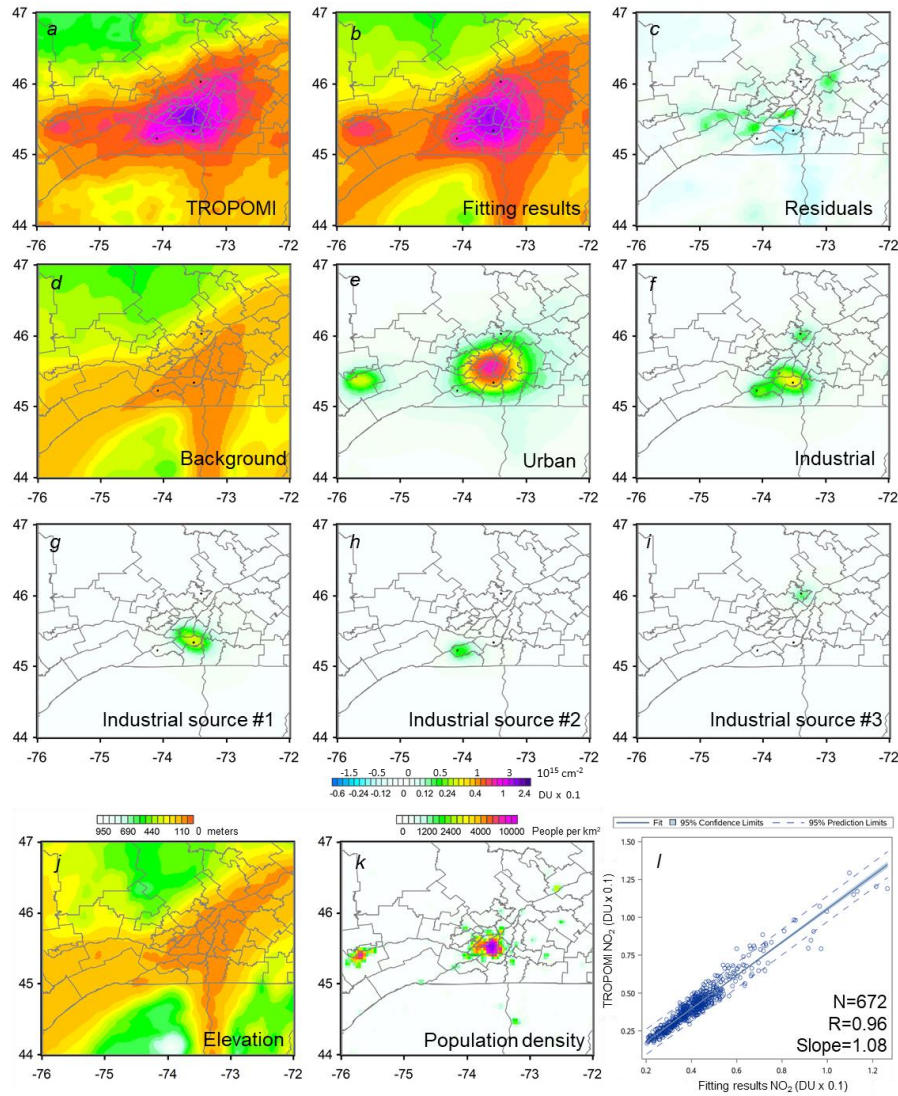


**Figure 3.** (a) Mean TROPOMI NO<sub>2</sub> for March 16– June 15, 2018-2019, over the Montreal area, (b) the fitting results and (c) the residuals (i.e., the difference between (a) and (b)). Tropospheric NO<sub>2</sub> VCDs have a large “background” level that is reflected by (d) the elevation-related component. (e) The population density-related and (f) industrial sources-related components. Panel (b) is the sum of panels (d), (e) and (f). Emission point sources are shown by the black dots and the airport by the slightly larger gray dot. The industrial sources-related component is comprised of three clusters: one (g) with two sources and two (h, i) with one source each. The data are smoothed by the oversampling technique with the averaging radius R=10 km. Proxies used by the statistical model (Eq. 1): (j) Elevation map on the colour scale that is similar to that for the elevation-related (“background”) component; (k) population density map. (l) Mean TROPOMI values (panel a) vs. the fitting results (panel b). Each dot represents the mean value for a cell on 0.2 by 0.2 grid for 2018 or 2019. The number of data points (N), the correlation coefficient (R) and the slope are also shown.



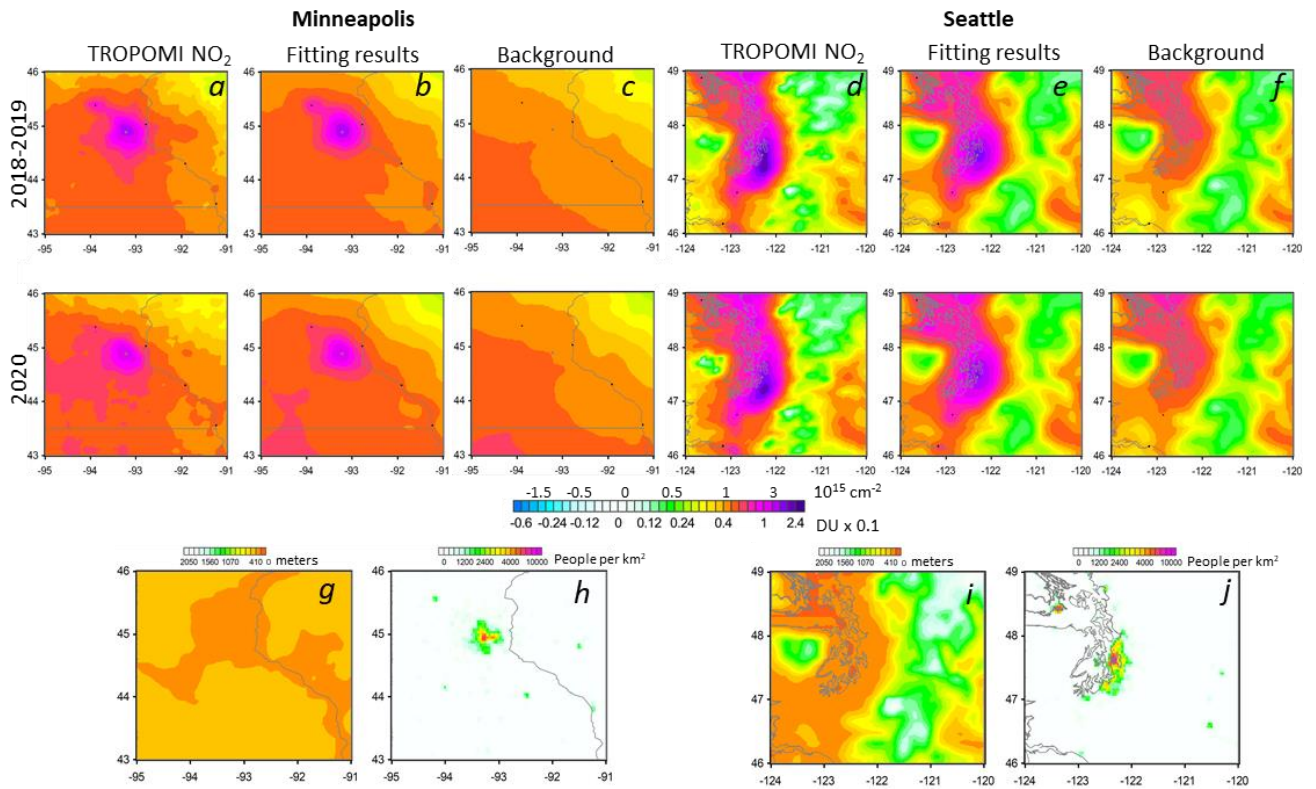


**Figure 4.** Mean TROPOMI NO<sub>2</sub> for March 16 – June 15 over a flat area around Minneapolis and mountain area around Seattle as indicated. The columns represent: mean TROPOMI NO<sub>2</sub> values, (column *a, d*), the fitting results (*b, e*), and the elevation-related background component (*c, f*). Elevation map on the colour scale that is similar to the background component (*g, i*) and the population density maps (*h, j*). The “hotspots” on the population density maps correspond to Minneapolis (*h*) and Seattle (*j*).

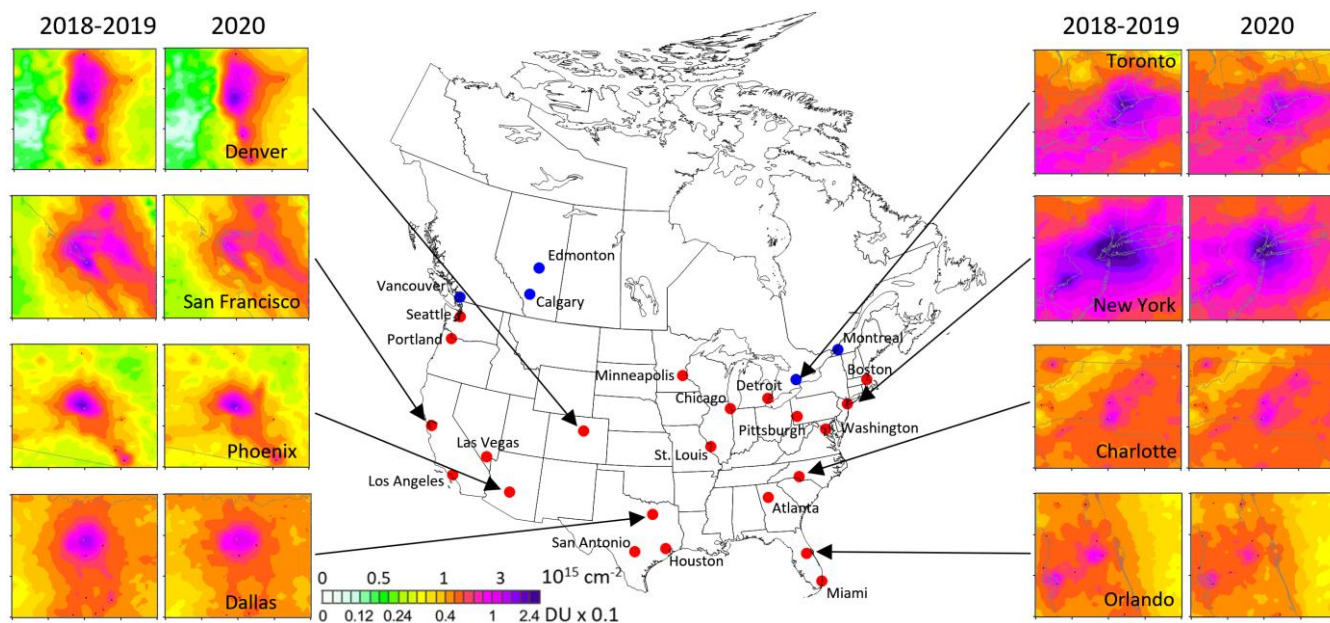


**Figure 5.** The map of locations of the analysed 27 most populated urban cites in (red) the US and (blue) Canada (22 and 5 areas respectively). The analysis was done for 3° (latitude) by 4° (longitude) areas around the sites. The mean NO<sub>2</sub> values for eight areas for the period from March 16 to June 15 in 2018-2019 and 2020 are also shown.

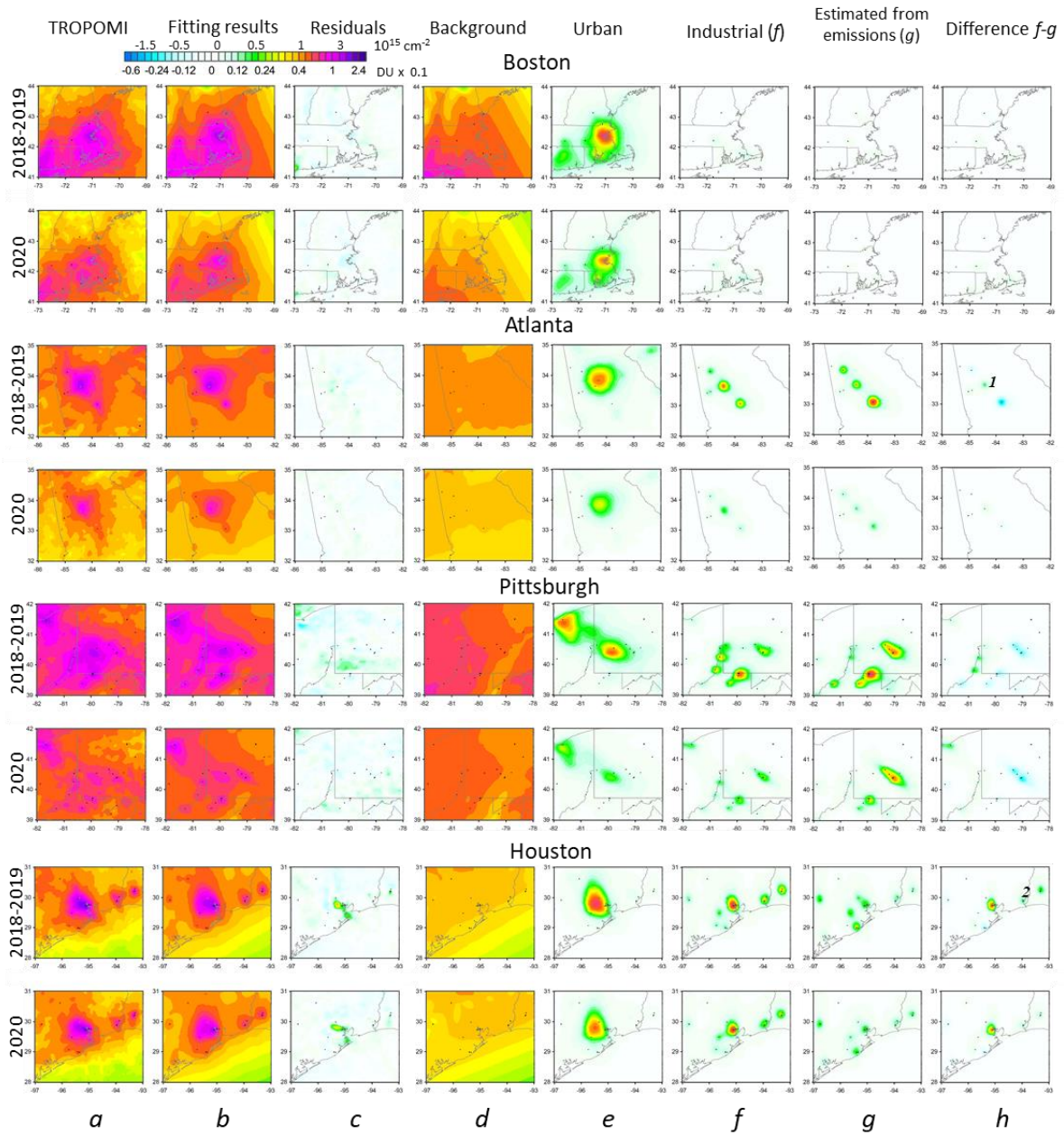


**Figure 6.** Mean TROPOMI NO<sub>2</sub> for March 16–June 15 over the four areas as indicated. For each area, the first row shows the 2018-2019 averages and the second row shown the 2020 averages. The columns represent: mean TROPOMI NO<sub>2</sub> VCD values, (column *a*), the fitting results (*b*), the residuals (*c*) as well as individual components of the fitting: the background (elevation-related) (*d*), the urban (population density-related) (*e*), and the industrial sources-related (*f*). VCDs estimated from reported emissions are in column (*g*) and the difference between columns *f* and *g* is in column *h*. 1- Hartsfield–Jackson Atlanta International Airport, 2- oil refineries near Houston.



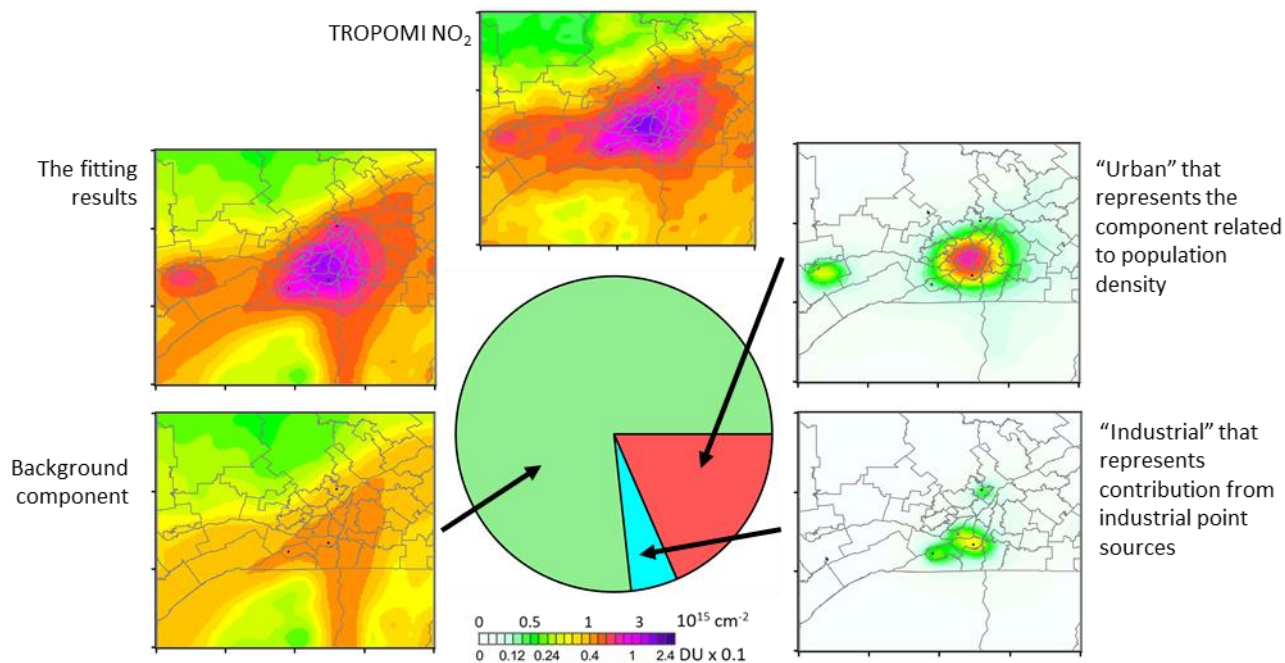


**Figure 7.** The contribution of the three components to the total NO<sub>2</sub> mass in the Montreal area for March 16 – June 15 (average for 2018-2019). The total mass can be represented as a sum of three components shown in Figure 2.

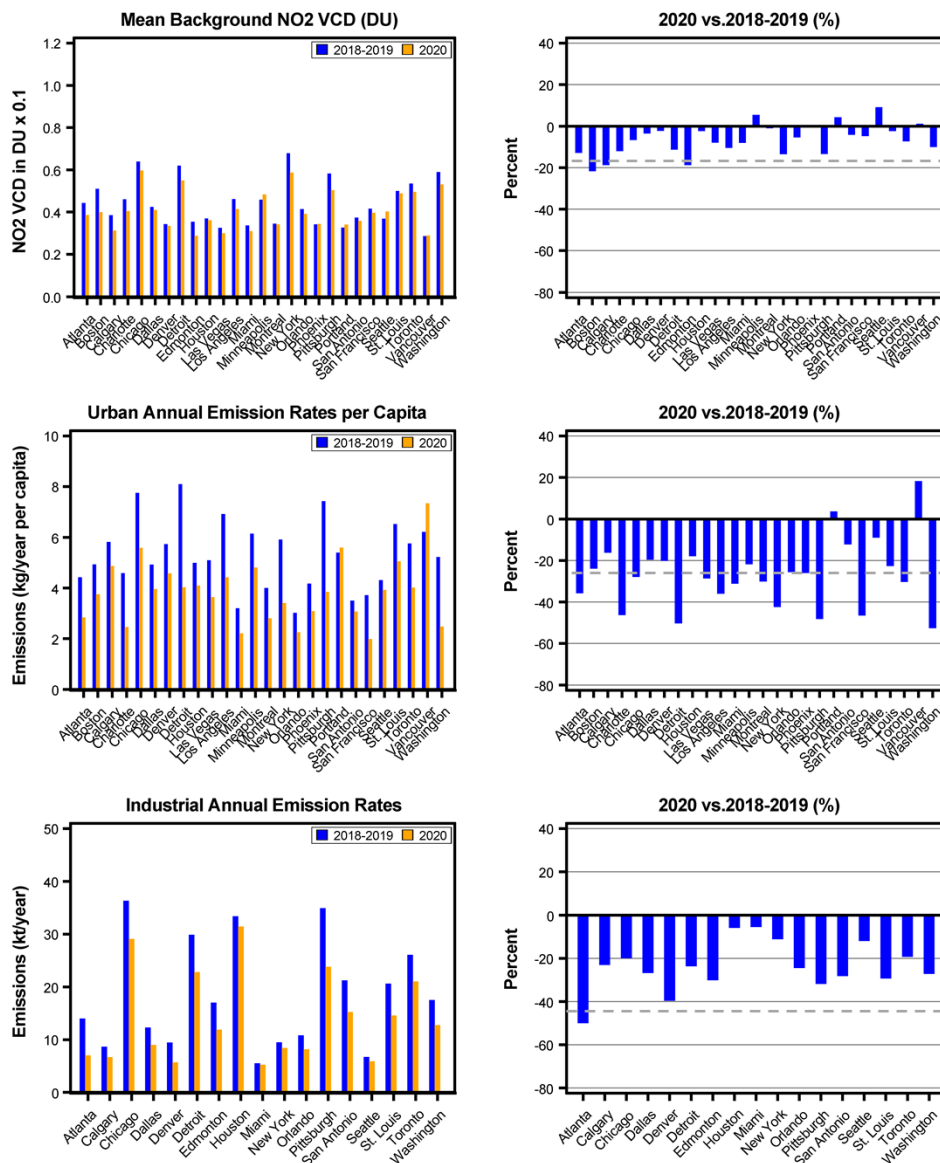
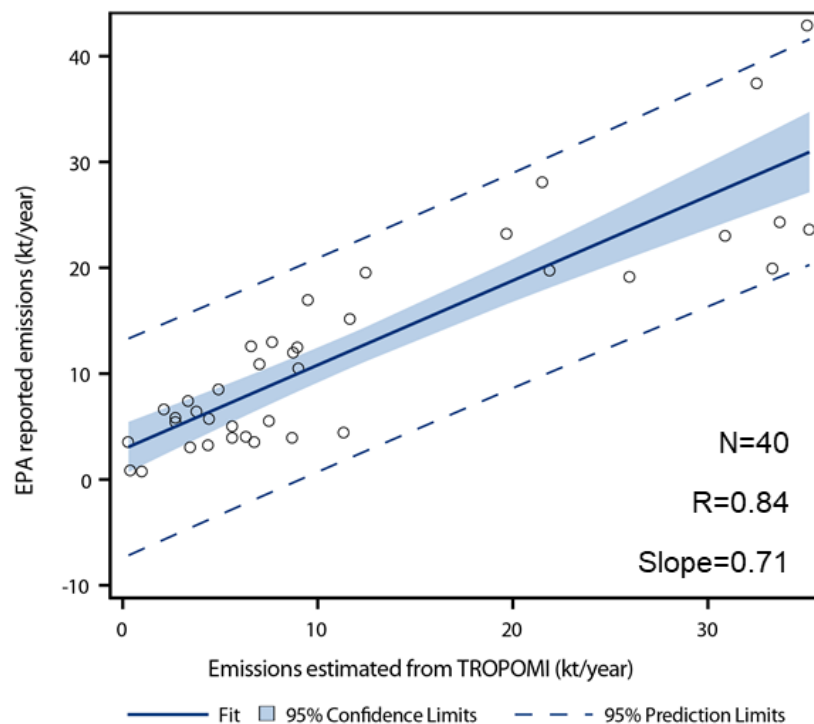
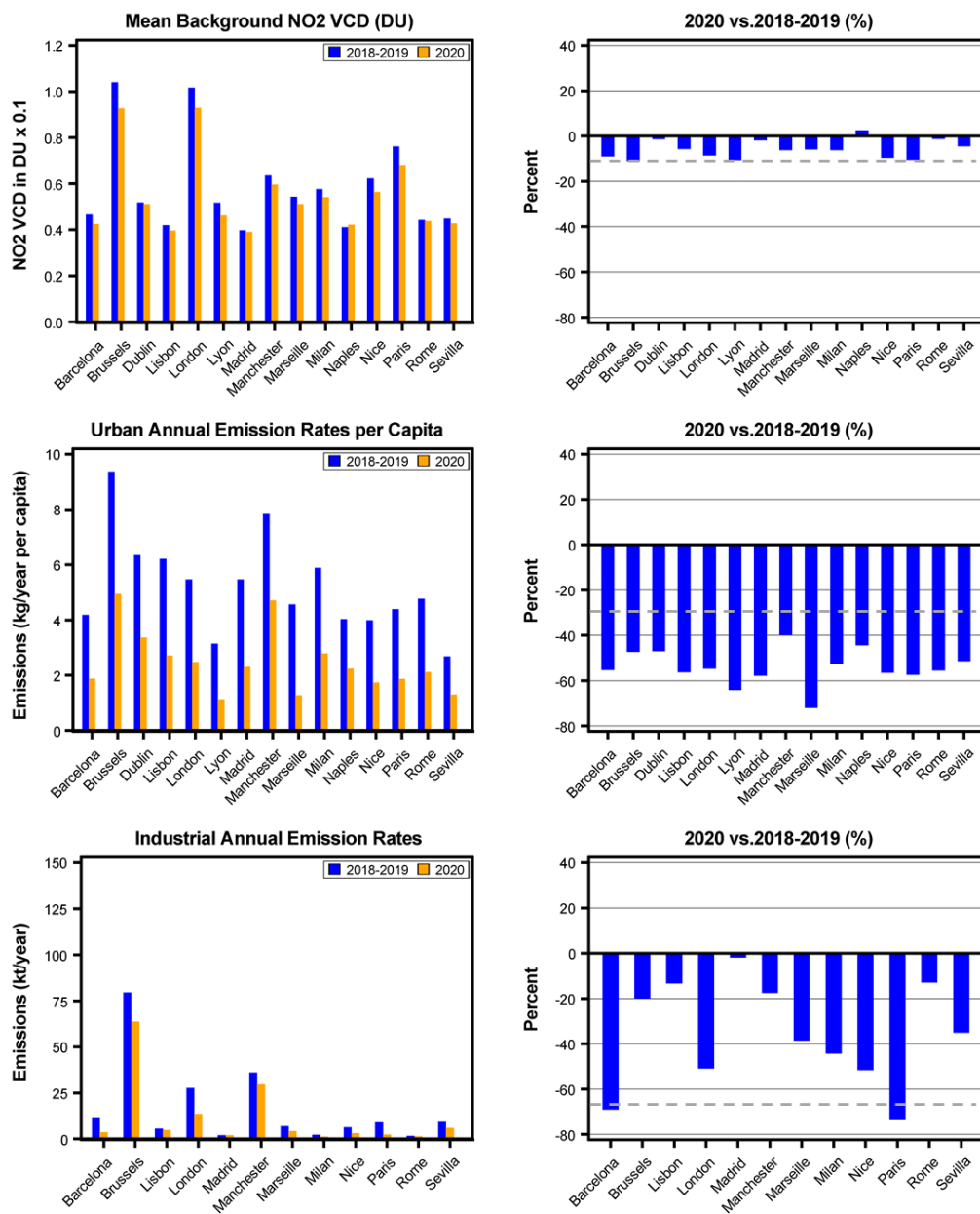


**Figure 8.** (left) The background (top row), urban (middle row), and industrial (bottom row) components for all 27 analysed areas in the U.S. and Canada in 2018-2019 (blue) and 2020 (orange). (right) The decline 2020 values in percent from the 2018-2019 values. The background component is expressed as the mean value of that component for the analysed area. The urban component is expressed as annual emissions per capita, and the industrial component is expressed as total emissions from the point sources for the period from March 16 to June 15. The grey dashed lines on the right panels indicate the 2- $\sigma$  level for the interannual variability.



5 **Figure 9.** Estimated and reported annual NO<sub>2</sub> emissions rates for U.S. sources for 2018-2019. Each dot represents the sum of all emissions in one urban area in 2018 or 2019 and there are 40 dots on the plot. The emissions are expressed as annual rates. The correlation coefficient between the two data sets is 0.84 and the slope is  $0.71 \pm 0.15$ . The standard deviation of the residuals is about  $5 \text{ kt y}^{-1}$ . The plot also shows the predicted regression line (blue), 95% confidence intervals for the regression mean (the shaded area), and 95% prediction intervals (dashed lines).

10



5 **Figure 10.** The same as Fig. 8, but for Europe-1 sub-region (Italy, France, Spain, Portugal, Belgium, Ireland, and UK).

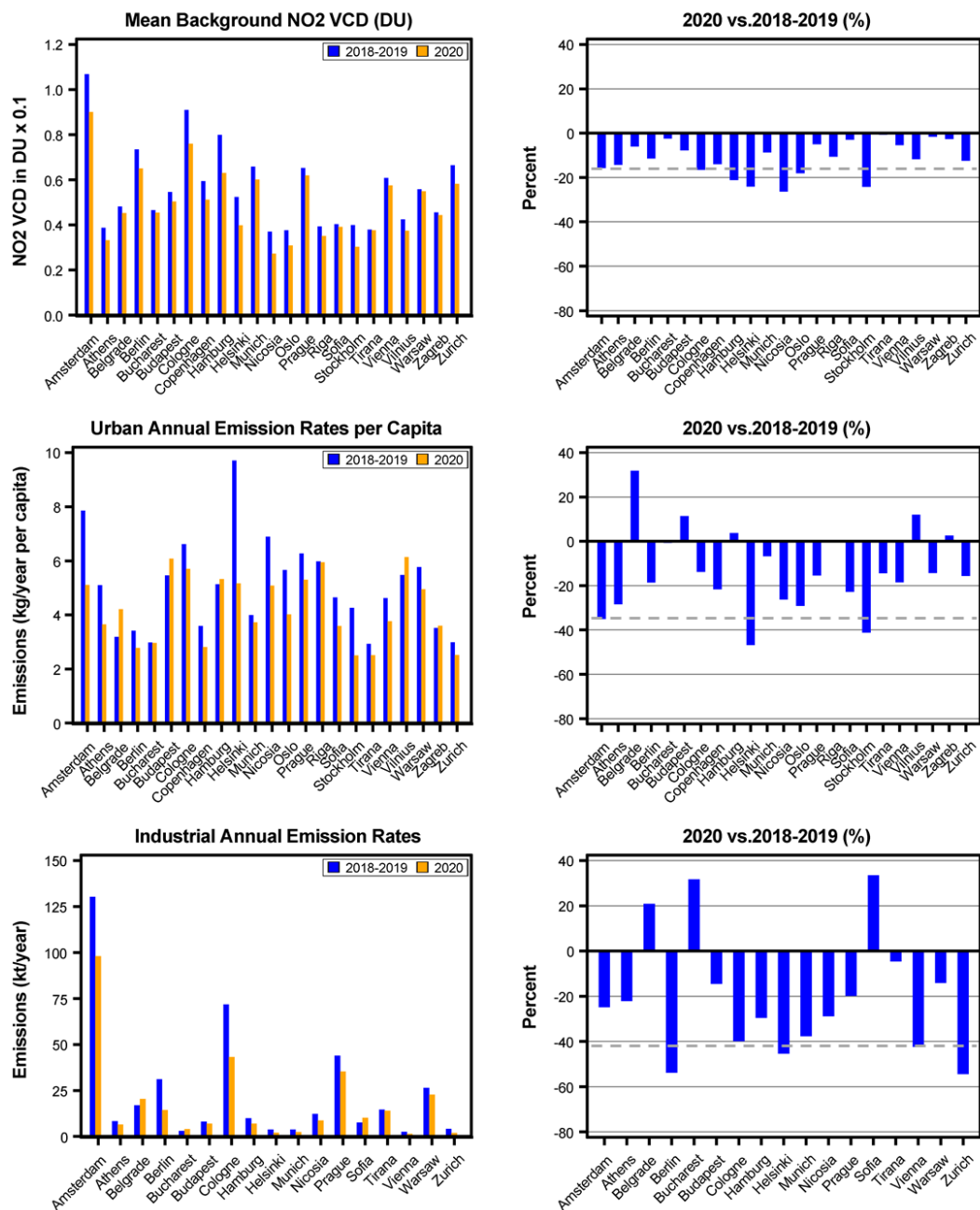


**Figure 11.** The same as Fig. 8, but for Europe-2 sub-region (other EU countries and non-members from former Yugoslavia).

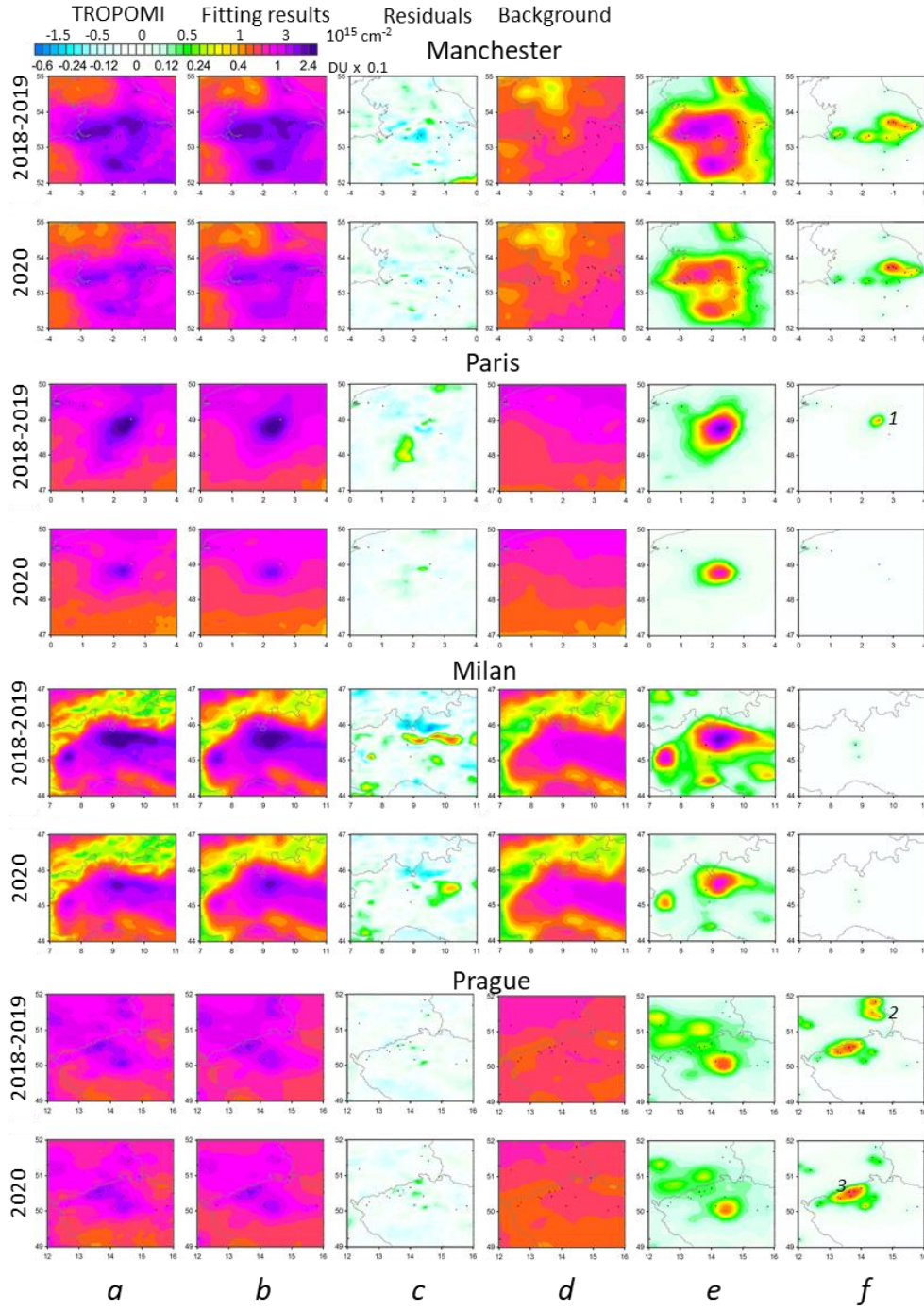
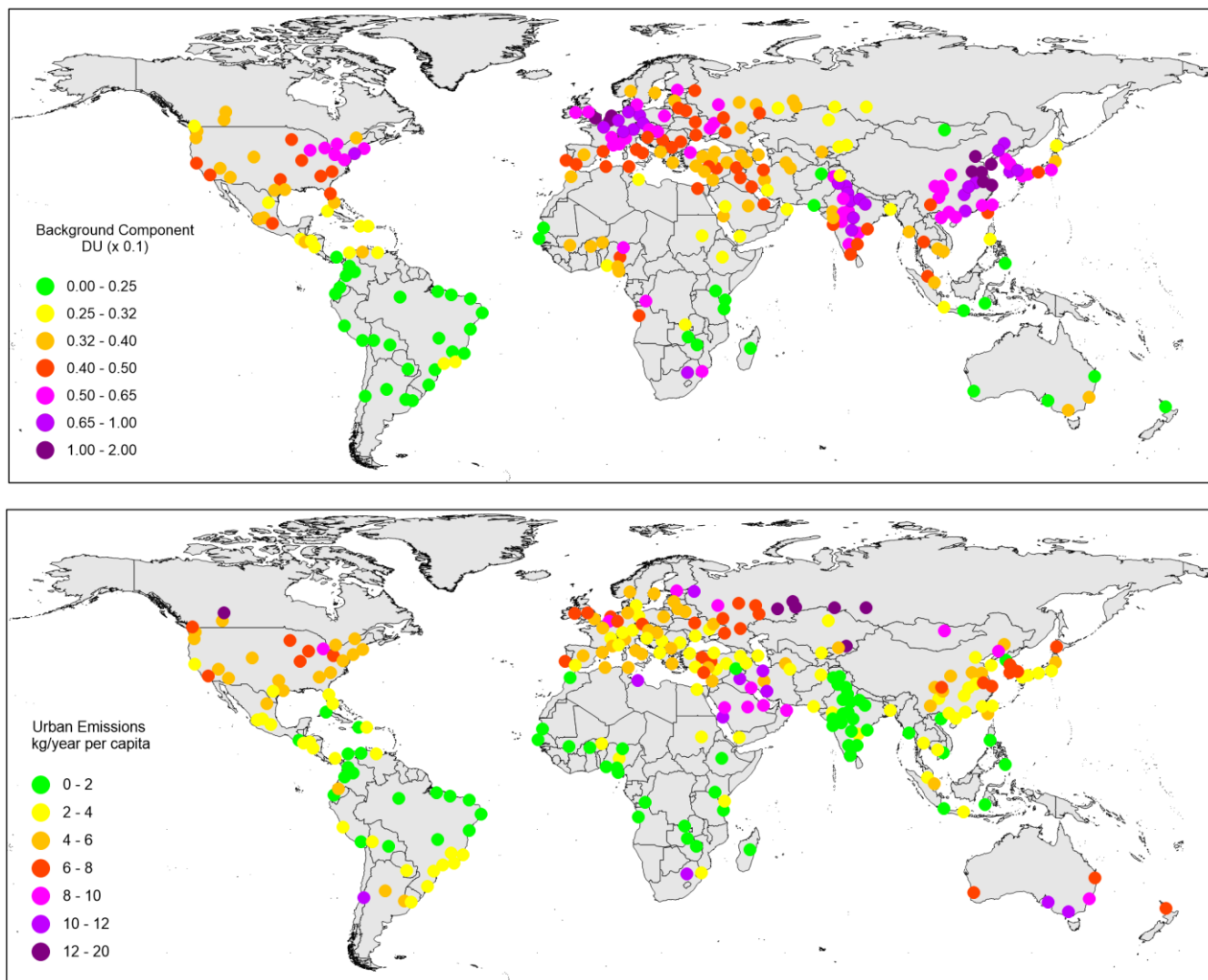


**Figure 12.** Similar to Figure 6 columns a-f, for areas around four European cities: Manchester, Paris, Milan, and Prague. 1- Charles de Gaulle Airport, 2- power plants in Germany, 3- power plants in Czech Republic.



5 **Figure 13.** (top) The map of the mean background component  $\text{NO}_2$  for all individual areas in 2018-2019 for the period March 16 – June 15 estimated from TROPOMI. (bottom) The map of annual per capita urban  $\text{NO}_2$  emissions for the same period. The analysis was done using estimates for cities with population greater than 6 million in China and 1 million for the rest of the world.



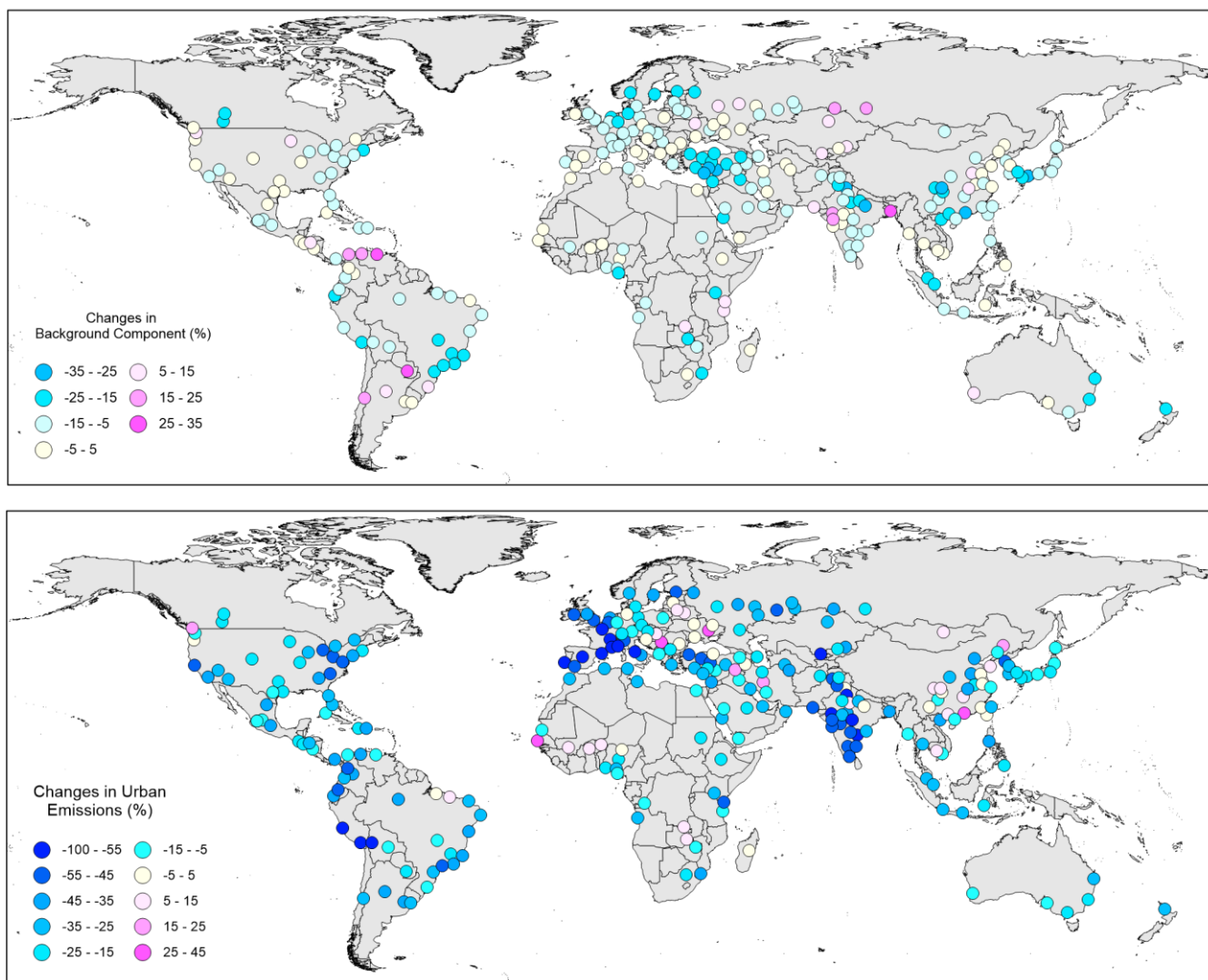


**Figure 14.** The map of NO<sub>2</sub> percent changes between 2018-2019 and 2020 for the period March 16 – June 15 estimated from TROPOMI data for (top) background component and (bottom) urban annual emissions per capita. The analysis was done using estimates for cities with population greater than 6 million in China and greater than 1 million for the rest of the world.



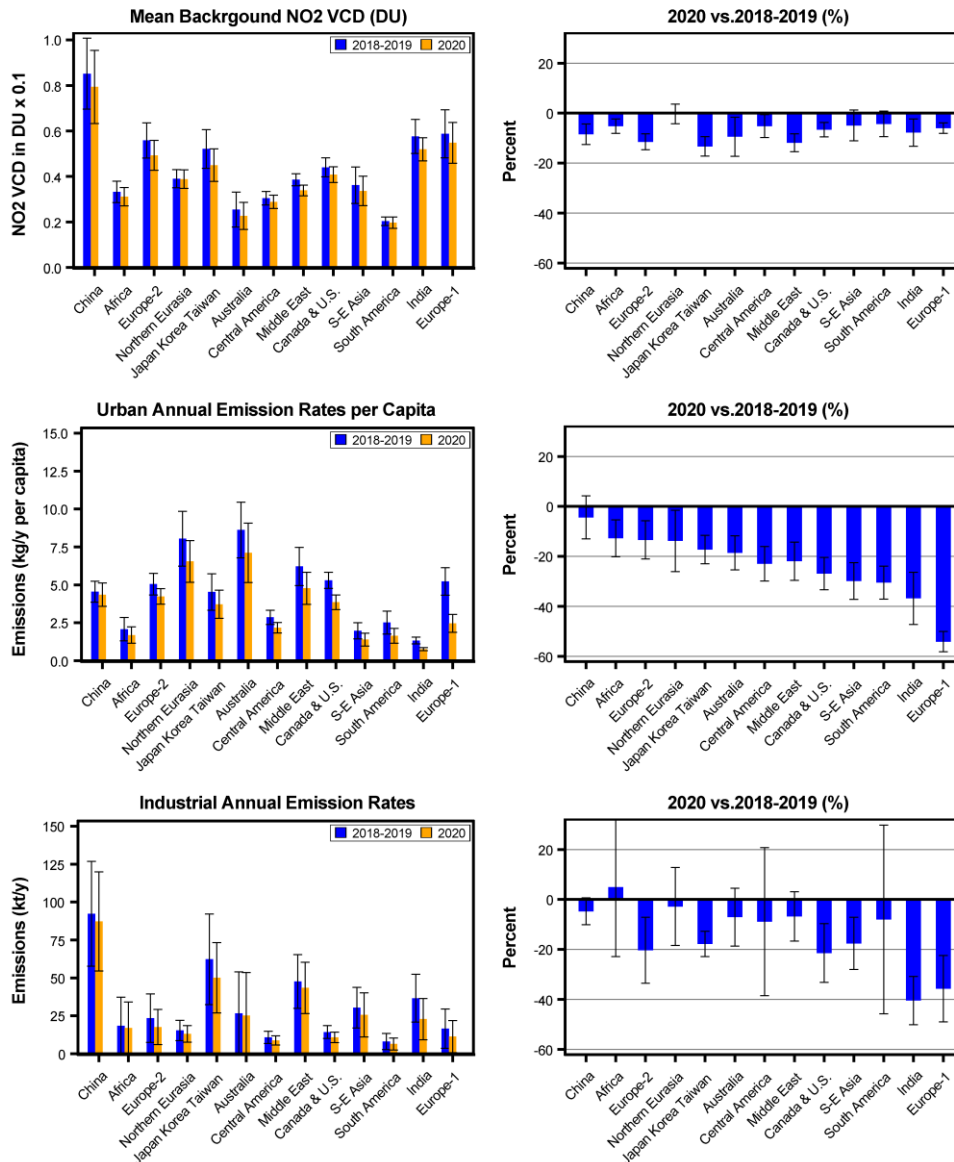


**Figure 15.** (left) The mean values for March 16–June 15 in 2018-2019 (blue) and 2020 (orange) values for (top) the background-, (middle) urban-, and (bottom) industrial components for the 13 regions. (right) The decline of 2020 mean values in percent from the mean 2018-2019 values. The data are sorted according to the changes between 2020 and 2018-2019 in the urban component (middle right panel). Mean values for each region were calculated as a mean of the values from all areas for that region. The uncertainty ( $\sigma$ ) was calculated as a standard error of the mean. The error bars represent  $2\sigma$  intervals.

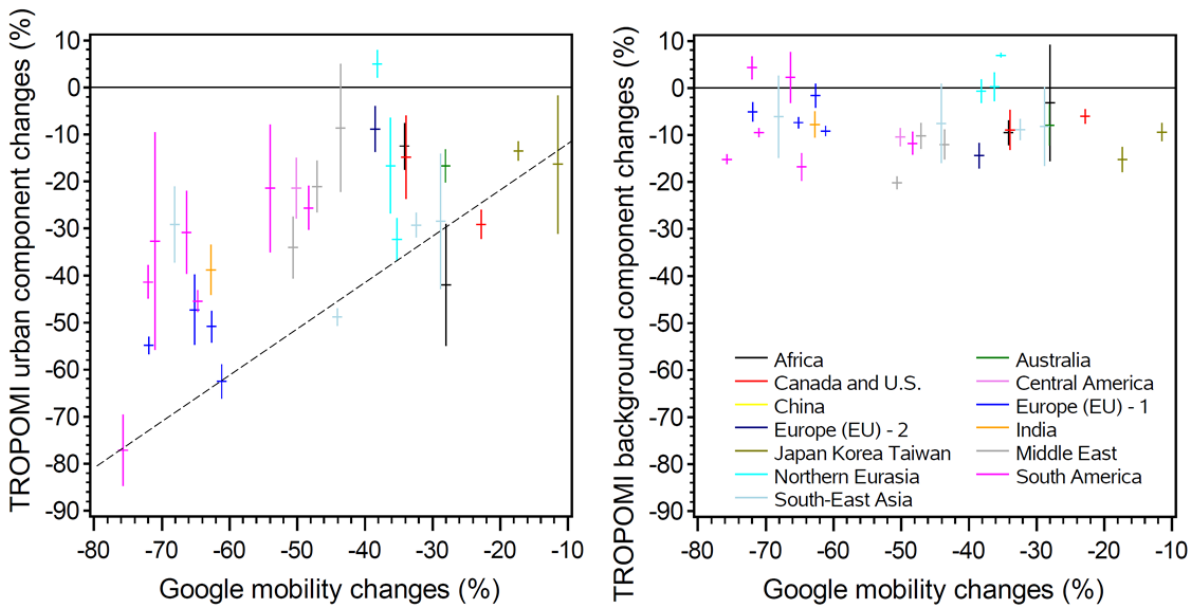


**Figure 16.** A scatter plot of Google mobility statistic changes vs. TROPOMI NO<sub>2</sub> VCD changes for (left) the urban and (right) background components during the period from March 16 to June 15, 2020 compared to the baseline period. The Google mobility statistic changes show the difference with the pre-lockdown period (Jan 3 – Feb 6, 2020) in percent. For TROPOMI, the difference is between the 2020 and the 2018-2019 average. Each symbol represents one country; the dot colour demonstrates the region as shown in the legend. Only countries with at least two cities used in this study are included in this plot. The correlation coefficient between the two data sets is 0.62. The dashed  $Y=X$  line is shown for reference. The error bars represent the standard errors.